

## Cosmological constraints on the multiscalar field dark matter model

L. O. Téllez-Tovar<sup>\*</sup>

*Departamento de Física, Centro de Investigación y de Estudios Avanzados del IPN,  
A.P. 14-740, 07000 México D.F., México  
and Instituto de Ciencias Físicas, Universidad Nacional Autónoma de México,  
A.P. 48-3, 62251 Cuernavaca, Morelos, México*

Tonatiuh Matos

*Departamento de Física, Centro de Investigación y de Estudios Avanzados del IPN,  
A.P. 14-740, 07000 México D.F., México*

J. Alberto Vázquez<sup>†</sup>

*Instituto de Ciencias Físicas, Universidad Nacional Autónoma de México,  
A.P. 48-3, 62251 Cuernavaca, Morelos, México*



(Received 14 June 2022; accepted 21 October 2022; published 1 December 2022)

The main aim of this paper is to provide cosmological constraints on the multiscalar field dark matter model, in which we assume the dark matter is made up of different ultralight scalar fields. As a first approximation, we consider they are real and do not interact with each other. We study the equations for both the background and perturbations for  $N$ -fields and present the evolution of the density parameters, the mass power spectrum, and the cosmic microwave background spectrum. In particular, we focus on two scalar fields with several combinations for the potentials  $V(\phi) = 1/2m_\phi^2\phi^2$ ,  $V(\phi) = m_\phi^2f^2[1 + \cos(\phi/f)]$ , and  $V(\phi) = m_\phi^2f^2[\cosh(\phi/f) - 1]$ , however, the work, along with the code, could be easily extended to more fields. We use the data from baryon acoustic oscillation, big bang nucleosynthesis, Lyman- $\alpha$  forest, and supernovae to find constraints on the sampling parameters for the cases of a single field and double field, along with the Bayesian evidence. We found that some combinations of the potentials get penalized through the evidence, however, for others there is a preference as good as for the cold dark matter.

DOI: [10.1103/PhysRevD.106.123501](https://doi.org/10.1103/PhysRevD.106.123501)

### I. INTRODUCTION

So far the most accepted cosmological model considers the contribution of cold dark matter (CDM) as a key component for structure formation, along with a cosmological constant ( $\Lambda$ ), as the simplest form of dark energy. The success of this model, known as  $\Lambda$ CDM, relies mainly on the accurate agreement with several cosmological observations, for example, measurements of the current accelerated expansion of the Universe and the cosmic microwave background radiation (CMB). The best description for the dark matter assumes it to be made up of pressureless, nonrelativistic, neutral, and nonbaryonic particles whose interaction is primarily through gravity. However, the assumption of a particle with these properties brings up many unexplained features, mainly at Galactic scales, i.e., the central density behavior in Galactic halos or the overpopulation of substructures at small scales; for an extended review about the problems and possible solutions,

see Refs. [1,2]. Recent studies suggest there is no longer a missing satellites problem, however, there could be a problem with so many satellites, see [3,4]. An alternative that may alleviate these problems is to consider a dark matter but now described by a single scalar field  $\phi$  with an associated potential  $V(\phi)$ , whose evolution is carried out by the Klein-Gordon equation. The idea of assuming a scalar field as the dark matter (DM) of the Universe was introduced about two decades ago, where the simplest possibility is to be real, or complex, minimally coupled to gravity, and interacting with ordinary matter only gravitationally [5–8]. Throughout the years, this model has been rediscovered and received many names, for example: scalar field DM (SFDM) [7], fuzzy DM [9], Bose-Einstein condensate DM [10], and, more recently, ultralight axion DM [11]; here we will refer to it as SFDM, as it was named in [8]. Based on this idea, the particle associated with the field is an ultralight boson whose mass oscillates around  $m_\phi \sim 10^{-22}$  eV and hence is able to form Bose-Einstein condensates that conform the Galactic structures [11–15]. In this work, we will consider that the scalar field (or fields) are already formed and we will not delve into their origin; see Refs. [11,16] for details.

<sup>\*</sup>ltellez@fis.cinvestav.mx

<sup>†</sup>jvazquez@icf.unam.mx

For an expanding universe, the scalar field cools down along with the expansion, and after a while, this causes the field, the boson gas, to freeze and then condensate. For an ideal boson gas the condensation temperature goes like  $T_c \sim m^{-5/3}$ , implying that for a mass big enough the condensation temperature becomes small, but the opposite happens if the mass turns out to be light, or ultralight, and the condensation temperature could be very high. However, after the turn around, the structures start forming and the recollapse raises the temperature of the bosons again. Therefore, depending on the initial conditions of the galaxy formation, the boson particles can produce excited states, although most of the boson particles remain in the condensate state or in the ground state [12–14,17,18]. These excited particles can be interpreted as other scalar fields. Thus, once the galaxy is already formed, if it still contains boson particles in several quantum states, then it can be interpreted as a galaxy with different scalar fields. On the other hand, for heavy particles these vibrations could be neglected; however, for ultralight particles an excitation could be comparable with its original mass. In an effective way, the scalar field contains the mass plus the effective mass of the excitation's energy. Thus, this boson gas of particles in excited states could be seen effectively as many scalar fields with different potentials, hence the introduction of the multiscalar field dark matter model.

Another motivation to introduce several scalar fields with different potentials could be encouraged because if 4% of just the baryonic matter in the universe is so diverse, then we can suspect that 26% of the matter, the dark matter, could be made of several species with different properties too. This diversity of particles could be observed and be tested at various scales, for instance, at the galactic level by observing the rotation curves as well as at the largest scales of the Universe. If the dark matter is formed of scalar fields, then both results should match flawlessly. In this work, we will focus on the cosmological implications, leaving for a parallel work the study of astrophysical features [19].

It has been shown that a scalar field with a convex potential behaves, on average, like dust during late times and hence mimics the behavior of the cold dark matter. However, depending on the specific form of the potential and even whether the field is real or complex, it may have different behaviors before acting like a pressureless fluid. So, in order to have a dark matter evolution, it is necessary that the dependence of the potential with respect to the field is such that it presents a minimum value at some critical point around which the field oscillates [11,15,20]. Some examples of such kinds of potentials are the parabolic function  $V(\phi) = 1/2m_\phi^2\phi^2$  [13,14,21] and the self-interacting potential with a quartic term contribution  $V(\phi) = 1/2m_\phi^2\phi^2 + \lambda_\phi\phi^4$  [16,22–24] or the axionlike potential  $V(\phi) = m_\phi^2 f^2 [1 + \cos(\phi/f)]$  [25–27] and its analog  $V(\phi) = m_\phi^2 f^2 [\cosh(\phi/f) - 1]$  [28,29]. Here  $m_\phi$  is interpreted as the

mass of the field,  $\lambda_\phi$  is the self-interacting constant, and  $f$  represents a decaying constant. For a single field, several constraints on its mass have been imposed by using CMB and matter power spectrum [30], galactic dynamics [31], dwarf galaxies [32–34],  $N$ -body simulations with reionization process [35], and Lyman- $\alpha$  flux spectra [36,37]. However, the presence of small inconsistencies among datasets are also found, as can be seen in Fig. 1 of Ref. [16], as well as in Ref. [38]. This single field model provides a very good description of the evolution of the cosmological densities and the peaks of the CMB as well as the number of substructures in galaxy arrays, among others [11–15]. Nonetheless, it still presents some open issues [11]. For example, numerical simulations have shown that the mass of the field could vary for different scales of the simulation in order to fit the observations, for instance on the formation of galaxies [39], the whirling plane of satellite galaxies around the Milky Way, Andromeda, and Centaurus A galaxies [40], the same mass scale in satellite galaxies of the Milky Way [41], or the  $\sigma_8$  and  $H_0$  tension [42,43], just to mention a few.

In this work, to alleviate these discrepancies, we open up the possibility that the dark matter may be composed of several types of scalar fields. That is, the main aim of this work is to present a model where the dark matter may be made up by several scalar fields, with different potentials, and to show its constraints imposed by current cosmological observations. This model may help us to alleviate the inconsistencies among the constrictions of the mass values obtained by different observations, arguing that they could be different dark matter particles [44]. Also, if we consider two scalar fields with different masses, the same mass scale in the satellite galaxies of the Milky Way could be explained, i.e., one type of particle could form the host galaxy and the other the satellites [45]. We will refer to this model as the multiscalar field dark matter (MSFDM). Other areas have included similar ideas where two or more fields are used, for instance a combination of the inflaton and the SFDM [16], two scalar fields as dark energy [46,47], the inflaton and the curvaton [48], two scalar fields for inflation [49,50], interactions between dark energy and dark matter [51], or the axiverse model [44,52,53] (see also [54]).

Given the motivations above, in this paper we study the background dynamics and the linear perturbations of the model. As a first approximation we consider the scalar fields are spatially homogeneous, real, and with no interaction among each other, however, this part could be easily extended in future works. The paper is organized as follows: In Secs. II A and II B, we present the equations for the background and linear perturbations. In Sec. II C, the evolution is obtained with a modified version of the CLASS code for the background, mass power spectrum, and CMB power spectrum for different combinations of potentials. In Sec. III, we show the model constraints obtained

with a modified version of the MONTE PYTHON code, and finally in the last section we present our conclusions.

## II. MATHEMATICAL BACKGROUND

### A. Background dynamics

Throughout this paper, we base our analysis on a flat universe filled up with the standard components: baryons, dark energy in the form of a cosmological constant ( $\Lambda$ ), photons and neutrinos as relativistic species, and DM. For the neutrinos, we consider the base model used in [55], in which they assumed a normal mass hierarchy [56–59], two massless neutrinos, and a massive one with the minimal mass  $\sum m_\nu = 0.06$  eV. In particular, we assume the DM is described by multiple real scalar fields  $\phi_i$  endowed with their corresponding potentials  $V_i(\phi_i)$ , whereas the rest of the matter components are modeled as perfect fluids. Assuming a Friedmann-Lemaître-Robertson-Walker metric, the equations of motion for the background dynamics are

$$H^2 = \frac{\kappa^2}{2} \left( \sum_I \rho_I + \sum_i \rho_{\phi_i} \right), \quad (1a)$$

$$\dot{\rho}_I = -3 \frac{\dot{a}}{a} (\rho_I + p_I), \quad (1b)$$

$$\ddot{\phi}_i = -3H\dot{\phi}_i - \partial_{\phi_i} V_i(\phi_i). \quad (1c)$$

Here, dots represent derivatives with respect to the cosmic time  $t$ ,  $H$  is the Hubble parameter,  $\kappa^2 = 8\pi G$ , and  $\rho_I$  and  $p_I$  are the energy density and pressure of the  $I$ th fluid species, respectively, whereas for the scalar fields we have the associated density and pressure given by the standard expressions

$$\rho_{\phi_i} = (1/2)\dot{\phi}_i^2 + V_i(\phi_i), \quad p_{\phi_i} = (1/2)\dot{\phi}_i^2 - V_i(\phi_i). \quad (2)$$

Notice that we are assuming different species of scalar fields, representing each one by the subindex  $i$  in the above equations. The Klein-Gordon equations (1c), for each of the fields, can be written in a more manageable form by using the following polar transformation [60]:

$$\frac{\kappa\dot{\phi}_i}{\sqrt{6}H} \equiv \Omega_{\phi_i}^{1/2} \sin(\theta_i/2), \quad \frac{\kappa V_i^{1/2}}{\sqrt{3}H} \equiv \Omega_{\phi_i}^{1/2} \cos(\theta_i/2), \quad (3a)$$

where  $\Omega_{\phi_i} \equiv \kappa^2 \rho_{\phi_i} / 3H^2$  represents the dimensionless density parameter, and similarly  $\theta_i$  is an angular degree of freedom directly related to the equation of state for each one of the fields,  $w_{\phi_i} \equiv p_{\phi_i} / \rho_{\phi_i} = -\cos \theta_i$ . Additionally, we define the potential variables  $y_{1i}$  and  $y_{2i}$  as

$$y_{1i} \equiv -2\sqrt{2} \frac{\partial_{\phi_i} V_i^{1/2}}{H}, \quad y_{2i} \equiv -4\sqrt{3} \frac{\partial_{\phi_i}^2 V_i^{1/2}}{\kappa H}, \quad (3b)$$

whose form depends on the potential for a particular field. The equivalence between the polar transformation and the fluid equations can be seen in [61,62].

As a proof of the concept, we focus our study on the following potentials:

$$V_i(\phi_i) = \begin{cases} m_{\phi_i}^2 f_i^2 [1 + \cos(\phi_i/f_i)] & \text{cos,} \\ (1/2)m_{\phi_i}^2 \phi_i^2 & \text{quadratic,} \\ m_{\phi_i}^2 f_i^2 [\cosh(\phi_i/f_i) - 1] & \text{cosh,} \end{cases} \quad (4)$$

and their possible combinations, with  $f_i$  being a characteristic energy scale for the scalar fields  $\phi_i$  and  $m_{\phi_i}$  its corresponding mass scale. It can be seen that the variables (3b) for the aforementioned potentials can be written as

$$y_{1i}^2 = 4 \frac{m_{\phi_i}^2}{H^2} - 2\lambda_{\phi_i} \Omega_{\phi_i}, \quad (5a)$$

$$y_{2i} = \lambda_{\phi_i} y_{1i}. \quad (5b)$$

Notice that the three functional forms in (4) can be compressed into a dimensionless parameter  $\lambda_{\phi_i} = 3/\kappa^2 f_i^2$ , which facilitates the numerical calculations. Positive values of  $\lambda_{\phi_i} > 0$  describe the cosine potential and negative ones  $\lambda_{\phi_i} < 0$  the cosh potential, whereas the quadratic case corresponds to  $\lambda_{\phi_i} = 0$  (for more details see [21,25,29]). Then, for each field, the associated Klein-Gordon equation (1c) is represented by the following set of coupled equations:

$$\theta_i' = -3 \sin \theta_i + y_{1i}, \quad (6a)$$

$$\Omega_{\phi_i}' = 3(w_{\text{tot}} + \cos \theta_i) \Omega_{\phi_i}, \quad (6b)$$

$$y_{1i}' = \frac{3}{2} (1 + w_{\text{tot}}) y_{1i} + \frac{1}{2} \lambda_{\phi_i} \Omega_{\phi_i}^{1/2} \sin \theta_i, \quad (6c)$$

with  $w_{\text{tot}} = \sum_I \Omega_I w_I + \sum_i \Omega_i w_i$ , where  $\Omega_I \equiv \kappa^2 \rho_I / 3H^2$  and  $w_I = p_I / \rho_I$ . The prime denotes derivative with respect to the number of  $e$ -folds  $N = \ln a$ , and for any given variable  $q$  we have the relationship  $\dot{q} = Hq'$ .

The initial conditions necessary to solve these equations can be seen in Eq. (2.16) of Ref. [21] for the quadratic case, for the cosine potential see Eq. (5) Ref. [25], and for the hyperbolic cosine see Eq. (2.6) in Ref. [29]. The main purpose in all cases is to match a given value of the density parameter  $\Omega_{\phi_i,0}$  at the present time with the initial values of the dynamical quantities  $(\theta_i, y_{1i}, \Omega_{\phi_i})_{\text{ini}}$  at early enough times (typically for a scale factor of the order of  $a_{\text{ini}} \simeq 10^{-14}$ ).

In general terms, the mass parameter  $m_{\phi_i}$  determines the start of the rapid oscillations of the field  $\phi_i$  around the minimum of the potential  $V_i$ , which happens at around  $H \simeq 3m_{\phi_i}$ . For  $\lambda_{\phi_i} \neq 0$ , Eq. (5a) becomes a constraint equation that must be satisfied by the field variables at all times, whereas for  $\lambda_{\phi_i} = 0$  it simply tells us that  $y_{1i} = 2m_{\phi_i}/H$ . In fact, one expects that at late times  $m_{\phi_i} \gg H$ , so that for the three cases in (4) the relation  $y_{1i} = 2m_{\phi_i}/H$  should be satisfied with high accuracy. Only for the case  $\lambda_{\phi_i} < 0$  (cosh potential) it is also necessary to impose the scaling solution during radiation domination:  $\Omega_{\phi_i} = -12/\lambda_{\phi_i}$  and  $\cos \theta_i = -1/3$ , and then the initial value of  $y_{1i}$  is calculated from Eq. (5a). Furthermore, the field mass  $m_{\phi_i}$  is not an independent parameter in this case, and it has been shown that the two parameters are related through [29]

$$\frac{m_{\phi_i}}{H_{\text{ini}}} = 1.5 \left[ \left( \frac{\lambda_{\phi_i}}{3} - 4 \right) \frac{\Omega_{\phi_i,0}}{\Omega_{r,0}} a_{\text{ini}} \right]^2, \quad (7)$$

with  $\Omega_{r,0}$  the present density parameter of relativistic species and  $a_{\text{ini}}$  the initial value of the scale factor.

### B. Linear density perturbations

We consider the linear perturbations for the scalar fields by expanding the field to the leading order, with  $\phi_i(\vec{x}, t) = \phi_i(t) + \varphi_i(\vec{x}, t)$ , where  $\phi_i(t)$  are the background fields described in the above section, whereas  $\varphi_i$  are the field linear perturbations. The perturbed metric, in the synchronous gauge is  $ds^2 = -dt^2 + a^2(t)(\delta_{lm} + h_{lm})dx^l dx^m$ , with  $h_{lm}$  being the tensor perturbations of the metric. Working in Fourier space, the perturbed Klein-Gordon equation for each field is given by

$$\ddot{\varphi}_i = -3H\dot{\varphi}_i - \left( \frac{k^2}{a^2} + \partial_{\phi_i}^2 V_i \right) \varphi_i - \frac{1}{2} \dot{h} \dot{\varphi}_i. \quad (8)$$

In Eq. (8),  $k$  is the comoving wave number,  $h$  is the trace of  $h_{lm}$ , and  $\dot{h}$  is known as the metric continuity. Following the idea presented for the background in the previous section, we use the polar variables [21,25]

$$\begin{aligned} \sqrt{\frac{2}{3}} \frac{\kappa \dot{\varphi}_i}{H} &= -\Omega_{\phi_i}^{1/2} e^{\alpha_i} \cos\left(\frac{\vartheta_i}{2}\right), \\ \frac{\kappa y_{i,1} \varphi_i}{\sqrt{6}} &= -\Omega_{\phi_i}^{1/2} e^{\alpha_i} \sin\left(\frac{\vartheta_i}{2}\right), \end{aligned} \quad (9)$$

where  $\alpha_i$  and  $\vartheta_i$  are the new perturbation quantities. If we define the new quantities

$$\begin{aligned} \delta_{0i} &= -e^{\alpha_i} \sin\left(\frac{\theta_i - \vartheta_i}{2}\right), \\ \delta_{1i} &= -e^{\alpha_i} \cos\left(\frac{\theta_i - \vartheta_i}{2}\right), \end{aligned} \quad (10)$$

where the density contrast is  $\delta_{\phi_i} \equiv \delta\rho_{\phi_i}/\rho_{\phi_i} = \delta_{0i}$ , then the perturbed Klein-Gordon equation (8) can be rewritten as

$$\begin{aligned} \delta'_{0i} &= - \left[ 3 \sin \theta_i + \frac{k^2}{k_{Ji}^2} (1 - \cos \theta_i) \right] \delta_{1i} \\ &+ \frac{k^2}{k_{Ji}^2} \sin(\theta_i) \delta_{0i} - \frac{1}{2} h' (1 - \cos \theta_i), \end{aligned} \quad (11a)$$

$$\begin{aligned} \delta'_{1i} &= - \left[ 3 \cos \theta_i + \left( \frac{k^2}{k_{Ji}^2} - \frac{\lambda_{\phi_i} \Omega_{\phi_i}}{2y_{1i}} \right) \sin \theta_i \right] \delta_{1i} \\ &+ \left( \frac{k^2}{k_{Ji}^2} - \frac{\lambda_{\phi_i} \Omega_{\phi_i}}{2y_{1i}} \right) (1 + \cos \theta_i) \delta_{0i} - \frac{1}{2} h' \sin \theta_i, \end{aligned} \quad (11b)$$

where we have introduced the Jeans wave number as  $k_{Ji}^2 = H^2 a^2 y_{1i}$ . Other quantities of interest are the perturbations for the energy density  $\delta\rho_{\phi_i}$ , pressure  $\delta p_{\phi_i}$ , and velocity divergence  $\Theta_{\phi_i}$ , which are

$$\delta\rho_{\phi_i} = \dot{\phi}_i \dot{\varphi}_i + \partial_{\phi_i} V \varphi_i, \quad (12a)$$

$$\delta p_{\phi_i} = \dot{\phi}_i \dot{\varphi}_i - \partial_{\phi_i} V \varphi_i, \quad (12b)$$

$$(\rho_{\phi_i} + p_{\phi_i}) \Theta_{\phi_i} = \frac{k^2}{a} \dot{\phi}_i \varphi_i. \quad (12c)$$

In terms of the new variables  $\delta_{0i}$  and  $\delta_{1i}$ , they are written as

$$\delta\rho_{\phi_i} = \delta_{0i} \rho_{\phi_i}, \quad (13a)$$

$$\delta p_{\phi_i} = (\delta_{1i} \sin \theta_i - \delta_{0i} \cos \theta_i) \rho_{\phi_i}, \quad (13b)$$

$$(\rho_{\phi_i} + p_{\phi_i}) \Theta_{\phi_i} = \frac{k^2 \rho_{\phi_i}}{a H y_{i,1}} [(1 - \cos \theta_i) \delta_{1i} - \sin \theta_i \delta_{0i}]. \quad (13c)$$

Again, depending on the value of  $\lambda_{\phi_i}$ , one recovers the perturbed equations of any of the three different potentials of this work (4). The initial conditions for the perturbations simply are  $\delta_{0\text{init}} = 0$  and  $\delta_{1\text{init}} = 0$ . It has been shown that the dynamical variables  $\delta_{0i}$  and  $\delta_{1i}$  quickly reach an attractor behavior driven by the nonhomogeneous term  $h'$  in Eqs. (11) [21,25,29].

### C. Numerical results

In this section, we show the background evolution, mass power spectrum (MPS), and CMB power spectrum for different combinations of potentials, obtained with a

modified version of the CLASS code that is able to deal with multiple scalar fields [21,25,63]. This version of the code is publicly available and can be found in [64]. We use the ratio  $R = \Omega_{\phi_{1,0}}/\Omega_{\text{DM},0}$  to parametrize the energy density of the scalar fields, where  $\Omega_{\text{DM},0} = \Omega_{\phi_{1,0}} + \Omega_{\phi_{2,0}} + \Omega_{\text{cdm},0}$  represents the current total dark matter contribution from the scalar fields sector. The combination of the fields is symmetric, then for reference we take  $\phi_1$  to define  $R$ ; otherwise if  $\phi_j$  is taken as reference we need to redefine  $R = \Omega_{\phi_j}/(\sum_i \Omega_{\phi_i} + \Omega_{\text{cdm}})$ . The mass values for the fields were taken from the references mentioned in the Introduction, in particular, those reported in [45], where the existence of at least two scalar fields with masses of  $10^{-22}$  and  $10^{-20}$  eV is proposed to explain the observations of the galaxy cores.

Throughout this work, we consider several combinations for the fields and combined them with the CDM as well. This is because, until now, the nature of the dark matter is not yet determined and several possibilities should be kept in mind. As the next approximation to the single field, here we assume two types of fields with different combinations of potentials as dark matter, however, once we have enough accurate data, the analysis (and the code) could be easily generalized to  $N$  different fields.

In the first combination, we assume the field one has  $V(\phi_1) = \frac{1}{2}m_{\phi_1}^2\phi_1^2$  while the rest of the dark matter density is conformed by CDM, therefore  $\Omega_{\phi_{2,0}} = 0$ . As we can see in the left panel of Fig. 1, the main difference in the background is the start of the scalar field oscillations due to the mass and  $R$  values. If  $R > 0.5$ , the oscillations approach those of a single scalar field, while if  $R < 0.5$  the oscillations are less evident until they disappear when  $R = 0$  (there is only CDM). In the mass power spectrum,

the right panel of the same figure, we notice the expected cutoff in small scales for the lightest mass values ( $m_{\phi_1} < 10^{-20}$  eV) but the behavior is lost for heavier masses ( $m_{\phi_1} > 10^{-20}$  eV) because the scalar field behaves like dust over the shown scales. Similar to the background, we found that the MPS of the combinations is bounded by the cases  $R = 1$  (only SFDM) and  $R = 0$  (only CDM). We can see an example of this in Fig. 1 for  $m_{\phi_1} = 10^{-22}$  eV (black line) and  $10^{-20}$  eV (blue line) with  $R = 0.2$  (dotted) and  $R = 0.8$  (dashed). For  $R = 0.8$ , the oscillations approach the case of a single SFDM but disappear for  $R = 0.2$ ; this is evident for  $m_{\phi_1} = 10^{-22}$  eV. In the same way, in the right panel, when  $R = 0.8$  the mass power spectrum shows a cutoff similar to the single case for both values  $m_{\phi_1} = 10^{-22}$  and  $10^{-20}$  eV, but it behaves like CDM (red solid line) for  $R = 0.2$ .

For the second combination, we assume two scalar fields with no CDM, both of them with a quadratic potential  $V(\phi_{1,2}) = \frac{1}{2}m_{\phi_{1,2}}^2\phi_{1,2}^2$  (see Fig. 2). We found that the total contribution to the background evolution, in particular, the oscillations of the fields, depends on the contribution of each one through  $R$  and are bounded by the oscillations of the lightest and the heaviest field, respectively. For the MPS, the cutoff is more evident when the lightest field accounts for the principal contribution to  $\Omega_{\text{DM},0}$  ( $m_{\phi_2} > m_{\phi_1}$  and  $R > 0.5$  or  $m_{\phi_2} < m_{\phi_1}$  and  $R < 0.5$ ), and the behavior is closer to single field models ( $R = 0$  or  $R = 1$ ) depending on the dominant field, as expected. In the left panel of Fig. 2 we show the total contribution of the fields to the background using  $m_{\phi_1} = 10^{-22}$  with  $m_{\phi_2} = 10^{-24}$  eV (green). The oscillations are more evident for  $R = 0.8$  (dashed) than for  $R = 0.2$  (dotted) and both of them are bounded by the single cases (solid). This is seen as

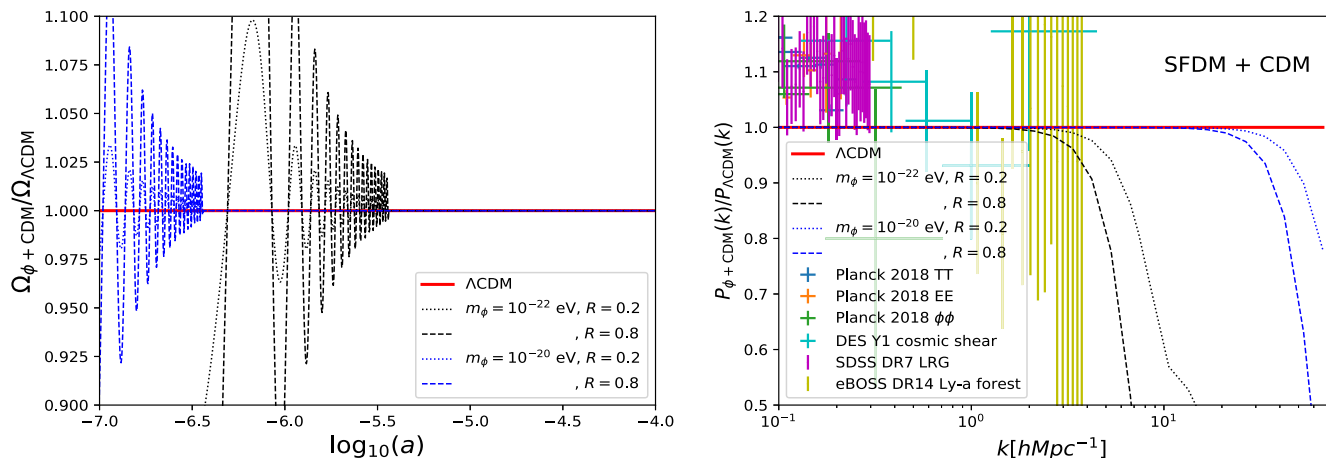


FIG. 1. Evolution, with early times enlarged, of the ratio of the density parameters  $\Omega_{\phi+\text{CDM}}/\Omega_{\Lambda\text{CDM}}$  (left) and the ratio of the linear matter power spectrum (right) at  $z = 0$ , for a SFDM + CDM model using  $\Lambda\text{CDM}$  as reference (solid red lines). The field potential is the quadratic one  $V(\phi) = \frac{1}{2}m_{\phi}^2\phi^2$ , and  $R$  represents the ratio of the field contribution to the total DM. Black lines represent a mass value of  $m_{\phi} = 10^{-22}$  eV while blue lines refer to  $m_{\phi} = 10^{-20}$  eV. Dashed and dotted lines represent  $R = 0.8$  and  $R = 0.2$  values, respectively. The data points for the MPS were obtained from [65].

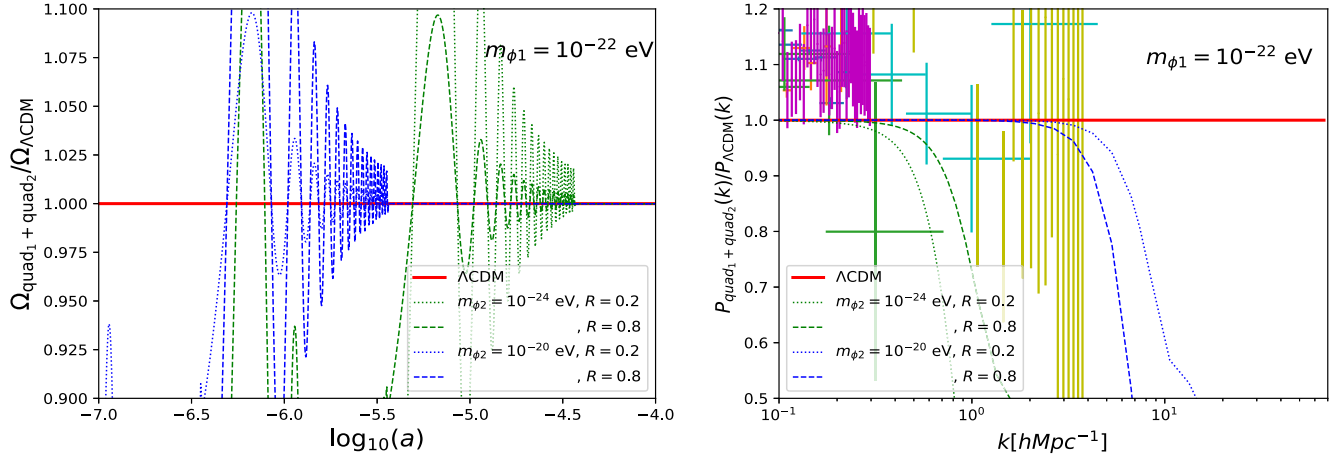


FIG. 2. Evolution, with early times enlarged, of the ratio of the density parameters  $\Omega_{\text{quad}_1+\text{quad}_2}/\Omega_{\Lambda\text{CDM}}$  (left) and the ratio of the linear matter power spectrum (right) at  $z = 0$ , for a double field model using  $\Lambda\text{CDM}$  as reference (solid red lines). The potential for both fields is the quadratic one  $V(\phi) = \frac{1}{2}m_\phi^2\phi^2$ , and  $R$  represents the ratio of the fields contribution to the total DM. Green lines represent a mass value of  $m_{\phi_2} = 10^{-24}$  eV and blue lines refer to  $m_{\phi_2} = 10^{-20}$  eV while  $m_{\phi_1}$  is fixed to  $10^{-22}$  eV. Dashed and dotted lines represent  $R = 0.8$  and  $R = 0.2$  values, respectively. The data points for the MPS were obtained from [65]. MPS data labels are the same as in Fig. 1.

well, but it is less noticeable due to the masses values, for the combination  $m_{\phi_1} = 10^{-22}$  with  $m_{\phi_2} = 10^{-20}$  eV (blue). For the MPS, we use the same values and we find a behavior similar to the previous case.

We also study a third combination of double field but now with  $V(\phi_1) = \frac{1}{2}m_{\phi_1}^2\phi_1^2$  and  $V(\phi_2) = m_{\phi_2}^2 f^2 [1 + \cos(\phi_2/f)]$ , respectively. For the background, we observe a similar behavior to that in the previous combinations, that is, once we kept the masses fixed and solely modified the

$\lambda_{\phi_2}$  values, we saw no difference among them. The oscillations of the fields depend on the masses and  $R$ , similar to the quadratic potentials case. See, for example, Fig. 3 where we take  $m_{\phi_1} = 10^{-22}$  eV along with  $m_{\phi_2} = 10^{-24}$  eV with  $\lambda_{\phi_2} = 10^4$  (green),  $m_{\phi_2} = 10^{-22}$  eV with  $\lambda_{\phi_2} = 10^5$  (black), and  $m_{\phi_2} = 10^{-20}$  eV with  $\lambda_{\phi_2} = 10^5$  (blue) for  $R = 0.2$  (dotted) and  $R = 0.8$  (dashed). For the MPS we see differences depending on  $m_{\phi_{1,2}}$  values or  $R$  and also by varying  $\lambda_{\phi_2}$  values. In order to see a bump in the

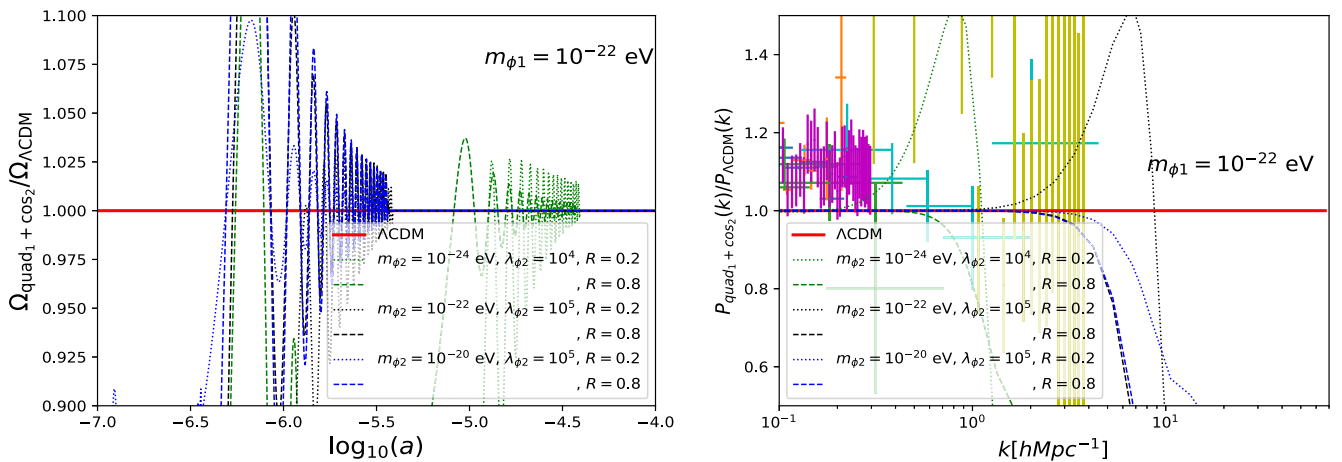


FIG. 3. Evolution, with early times enlarged, of the ratio of the density parameters  $\Omega_{\text{quad}_1+\text{cos}_2}/\Omega_{\Lambda\text{CDM}}$  (left) and the ratio of the linear matter power spectrum (right) at  $z = 0$ , for a model with two fields using  $\Lambda\text{CDM}$  as reference (solid red lines). Here, the field one has the potential  $V(\phi) = \frac{1}{2}m_\phi^2\phi^2$  with mass value  $m_\phi = 10^{-22}$  eV as reference, while the second field has  $V(\phi_2) = m_{\phi_2}^2 f^2 [1 + \cos(\phi_2/f)]$ . Green lines represent a mass value of  $m_{\phi_2} = 10^{-24}$  eV with  $\lambda_{\phi_2} = 10^4$ , black lines indicate  $m_{\phi_2} = 10^{-22}$  eV with  $\lambda_{\phi_2} = 10^5$ , and blue lines refer to  $m_{\phi_2} = 10^{-20}$  eV with  $\lambda_{\phi_2} = 10^5$ . Dashed and dotted lines represent  $R = 0.8$  and  $R = 0.2$  values, respectively, where  $R$  represents the ratio of the fields' contribution to the total DM. The data points for the MPS were obtained from [65]. MPS data labels are the same as in Fig. 1.

MPS, we need the second field to dominate ( $R < 0.5$ ) with lighter mass and higher  $\lambda_{\phi_2}$ . On the right side of Fig. 3, we can see the bump before the cutoff ( $k \sim 0.9$ ) for the green and black dotted lines, because in both cases the second field dominates and  $\lambda_{\phi_2}$  has high values with lighter masses. On the other hand, in the blue dotted line we do not observe the bump yet because the field becomes too heavy ( $m_{\phi_2} \geq 10^{-20}$  eV).

Finally, we study the combination of the field potential  $V(\phi_1) = \frac{1}{2}m_{\phi_1}^2\phi_1^2$  with  $V(\phi_2) = m_{\phi_2}^2f^2[\cosh(\phi_2/f) - 1]$ . In the background and MPS we have a similar behavior as before. This can be seen in Fig. 4 where we take the combination  $m_{\phi_1} = 10^{-22}$  eV,  $m_{\phi_2} = 1.54 \times 10^{-22}$  eV,  $\lambda_{\phi_2} = -8 \times 10^3$  (black),  $m_{\phi_1} = 10^{-22}$  eV,  $m_{\phi_2} = 0.6 \times 10^{-20}$  eV,  $\lambda_{\phi_2} = -5 \times 10^4$  (blue), and  $m_{\phi_1} = 10^{-22}$  eV,  $m_{\phi_2} = 0.3 \times 10^{-18}$  eV,  $\lambda_{\phi_2} = -4 \times 10^4$  (gray). It is important to note that both fields have the same contribution ( $R = 0.5$ ); other combinations require further analysis. In the mass power spectrum, at small scales, we see that  $\lambda_{\phi_2}$  has a greater contribution compared to the previous case because in the coshlike potential the scalar field mass depends on the  $\lambda_{\phi_2}$  value, contrary to the coslike potential in which these parameters are independent. When  $m_{\phi_2} \sim m_{\phi_1}$  we can appreciate a different behavior depending on the value of  $\lambda_{\phi_2}$ , for example, the black dotted line. However, if  $m_{\phi_2} \geq m_{\phi_1}$ , the change in  $\lambda_{\phi_2}$  does not display noticeable changes (blue and gray dotted lines).

In general for the background, we found slight differences at early times with respect to  $\Lambda$ CDM, where

the oscillations presented could give us information about how light the scalar field masses can be. We found too a cutoff at small scales in the mass power spectrum that differentiates our model from the CDM, and the shape below the cutoff depends on the multifield dynamics.

Regarding the CMB spectrum, when the mass of at least one of the fields, for any combination, is less than  $m_{\phi_i} < 10^{-26}$  eV, the spectrum of the fields differs from the  $\Lambda$ CDM spectrum as seen in [30]. However, for masses greater than  $m_{\phi_i} > 10^{-26}$  eV the same CMB power spectrum is obtained as for  $\Lambda$ CDM regardless of the value of  $\lambda_{\phi}$  or  $R$ . See, for example, Fig. 5 where we show the CMB power spectra for  $V(\phi_{1,2}) = \frac{1}{2}m_{\phi_{1,2}}^2\phi_{1,2}^2$  with  $m_{\phi_1} = 10^{-22}$  eV,  $m_{\phi_2} = 10^{-24}$  eV, and  $R = 0.8$  (green dashed line);  $V(\phi_1) = \frac{1}{2}m_{\phi_1}^2\phi_1^2$  with  $V(\phi_2) = m_{\phi_2}^2f^2[1 + \cos(\phi_2/f)]$  for  $m_{\phi_1} = 10^{-22}$  eV,  $m_{\phi_2} = 10^{-22}$  eV,  $\lambda_{\phi_2} = 10^5$ , and  $R = 0.2$  (black dotted line), and  $V(\phi_1) = \frac{1}{2}m_{\phi_1}^2\phi_1^2$  with  $V(\phi_2) = m_{\phi_2}^2f^2[\cosh(\phi_2/f) - 1]$  for  $m_{\phi_1} = 10^{-22}$  eV,  $m_{\phi_2} \propto 10^{-20}$  eV,  $\lambda_{\phi_2} = -5 \times 10^4$ , and  $R = 0.5$  (blue dotted line). For the three cases, we have obtained nearly the same CMB power spectra as for the  $\Lambda$ CDM model (solid red line). We also plotted the Planck 18 dataset as in Ref. [66].

### III. COMPARISON WITH DATA

In this section, we present the Bayesian inference procedure in order to constrain the MSFDM models by using different datasets. In order to perform the cosmological analysis, we generate Monte Carlo Markov chains

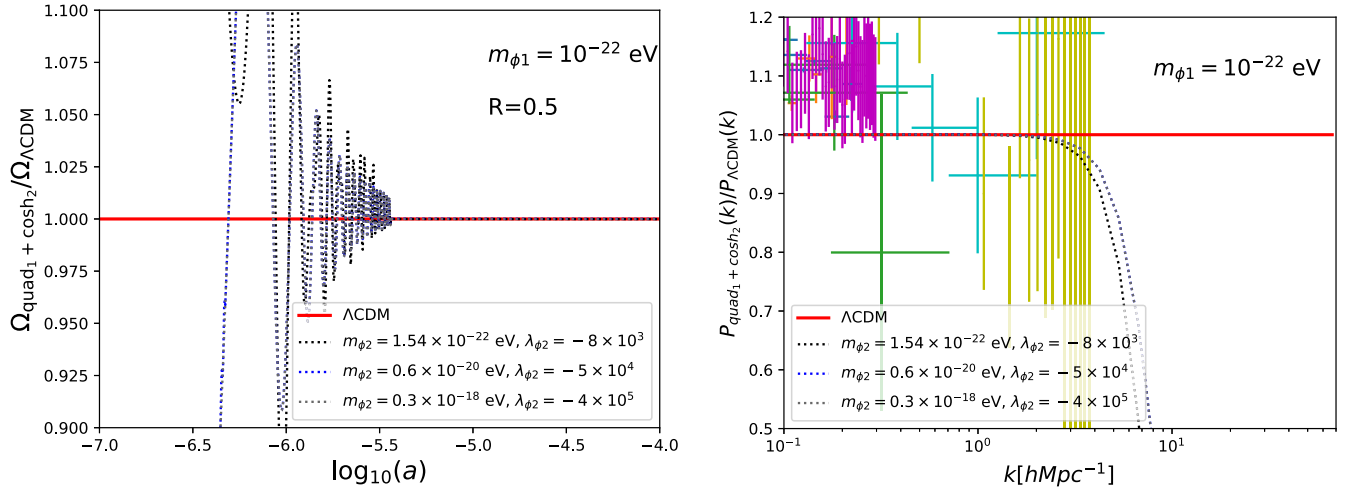


FIG. 4. Evolution, with early times enlarged, of the ratio of the density parameters  $\Omega_{\text{quad}_1 + \cosh h_2} / \Omega_{\Lambda\text{CDM}}$  (left) and the ratio of the linear matter power spectrum (right) at  $z = 0$ , for a model with two fields using  $\Lambda$ CDM as reference (solid red lines). The field one has the potential  $V(\phi) = \frac{1}{2}m_{\phi}^2\phi^2$  with mass value  $m_{\phi} = 10^{-22}$  eV as reference, and the second field has  $V(\phi_2) = m_{\phi_2}^2f^2[\cosh(\phi_2/f) - 1]$ . Black lines represent a mass value of  $m_{\phi_2} = 1.54 \times 10^{-22}$  eV with  $\lambda_{\phi_2} = -8 \times 10^3$ , blue lines indicate  $m_{\phi_2} = 0.6 \times 10^{-20}$  eV with  $\lambda_{\phi_2} = -5 \times 10^4$ , and green lines refer to  $m_{\phi_2} = 0.3 \times 10^{-18}$  eV with  $\lambda_{\phi_2} = -4 \times 10^5$ . Dotted lines represent  $R = 0.5$ , where  $R$  represents the ratio of the fields' contribution to the total DM. The data points for the MPS were obtained from [65]. MPS data labels are the same as in Fig. 1.

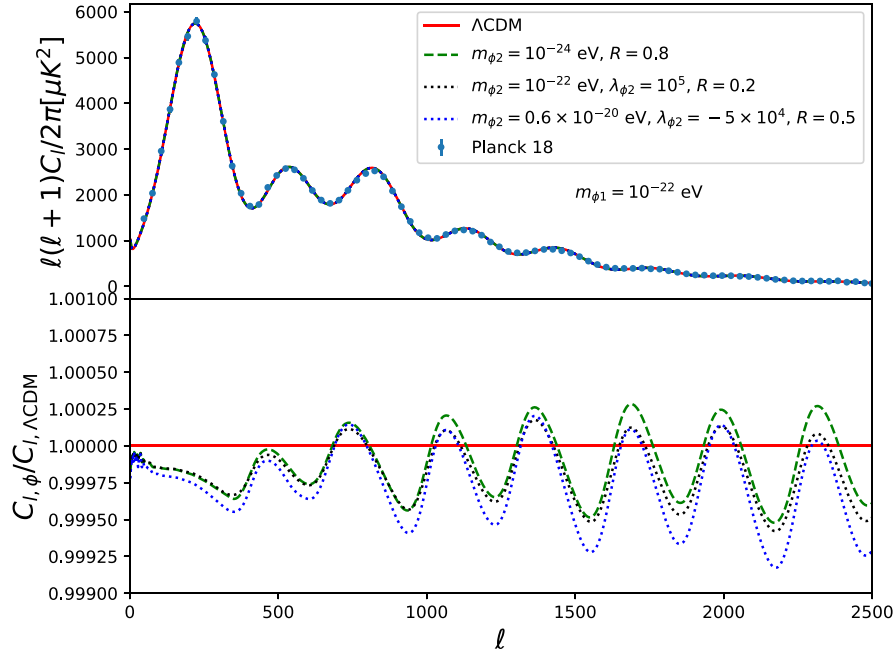


FIG. 5. The CMB power spectrum (upper) and the ratio (lower) using  $\Lambda\text{CDM}$  as reference (solid red lines), for  $V(\phi_{1,2}) = \frac{1}{2}m_{\phi_{1,2}}^2\phi_{1,2}^2$  (green dashed line),  $V(\phi_1) = \frac{1}{2}m_{\phi_1}^2\phi_1^2$  with  $V(\phi_2) = m_{\phi_2}^2f^2[1 + \cos(\phi_2/f)]$  (black dotted line), and  $V(\phi_1) = \frac{1}{2}m_{\phi_1}^2\phi_1^2$  with  $V(\phi_2) = m_{\phi_2}^2f^2[\cosh(\phi_2/f) - 1]$  (blue dotted line).

with the Metropolis-Hastings algorithm using a modified version of the MONTE PYTHON code [67,68] with the modified version of CLASS used in Sec. II C. We verified that our chains converged using the Gelman-Rubin criterion  $R - 1 < 0.03$  implemented in MONTE PYTHON. Then we discuss the merits of the models with respect to CDM within the framework of the Bayesian model selection. See [69] for a Bayesian inference review.

### A. Cosmological constraints

In the previous section we saw that the main difference throughout the models rests on the mass power spectrum at small scales, hence we use the 3D matter power spectrum inferred from Lyman- $\alpha$  data from the BOSS and eBOSS Collaborations [65]. We also use the Ly- $\alpha$  baryon acoustic oscillation (BAO) from eBOSS DR14 [70], the Galaxy BAO from DR12 [71], 6dFGS [72], and Sloan Digital Sky Survey (SDSS) DR7 [73], and the supernovae (SNe) Ia survey Pantheon [74] to improve the constraining power. As mentioned in [65], the process of inferring the MPS is model dependent, therefore we will consider the constraints obtained here as an approximation. On the other hand, we found that the parameter constraints describing the scalar field remain the same when incorporating the Planck 18 dataset. For this reason and to reduce computational time, we have only used the data already described. See Appendix C for further details.

The sampling parameters in the analysis are the physical baryon density parameter  $\omega_{b,0}$ , the logarithmic power

spectrum scalar amplitude  $\log(10^{10}A_s)$ , the scalar spectral index  $n_s$ , the Thomson scattering optical depth due to reionization  $\tau_{\text{reio}}$ , the scalar field masses  $m_{\phi_i}$ , the decay parameters  $\lambda_{\phi_i}$ , and, instead of the cold dark matter density parameter, we use the scalar field density parameters  $\Omega_{\phi_i,0}$ . However, we found from previous analysis that the posteriors of  $\log(10^{10}A_s)$ ,  $n_s$ , and  $\tau_{\text{reio}}$  do not present a change with respect to  $\Lambda\text{CDM}$ , therefore we will keep these parameters fixed (see Appendix C). The flat priors used for the remaining sampling parameters are as follows:  $H_0 = [10, 100]$  for the Hubble constant in  $\text{km s}^{-1} \text{Mpc}^{-1}$ ,  $\omega_{b,0} = [0.005, 0.1]$  for the physical baryon density, and  $\Omega_{\phi_{1,0}} = \Omega_{\phi_{2,0}} = [0, 1]$  for the scalar field density parameters today. For the scalar field parameters, we choose the priors to be consistent with the numerical results we found with CLASS, and since these parameters can take values of powers of 10, we chose a logarithmic base to efficiently cover the entire parameter space and reduce the computational cost. This means that we have  $\log_{10}(m_{\phi_i}/\text{eV}) = [-24, -17]$  for the scalar field masses,  $\log_{10}(\lambda_{\phi_i}) = [1, 6]$  for the parameter on the trigonometric cosine potential, and  $\lambda_{\phi_{i,\text{aux}}} = [-6, -1]$  for the hyperbolic cosine potential. For this case, we cannot use directly  $\log_{10}(\lambda_{\phi_i})$  because  $\lambda_{\phi_i} < 0$ , so in order to cover the parameter space we use the auxiliary variable  $\lambda_{\phi_{i,\text{aux}}}$  whose relation with  $\lambda_{\phi_i}$  is given by  $\lambda_{\phi_i} = -10^{-\lambda_{\phi_{i,\text{aux}}}}$ . In what follows, we will use  $\text{quad}_i$  to refer to the potential  $V_i(\phi_i) = (1/2)m_{\phi_i}^2\phi_i^2$ ,  $\text{cos}_i$  for  $V_i(\phi_i) = m_{\phi_i}^2f_i^2[1 + \cos(\phi_i/f_i)]$  and  $\text{cosh}_i$  for

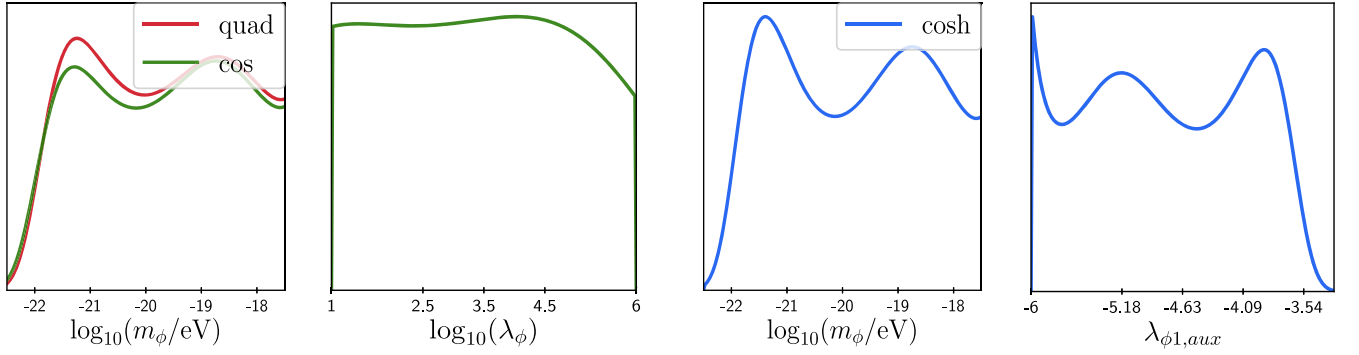


FIG. 6. 1D posterior distribution for the single SFDM with potentials  $V(\phi) = 1/2m_\phi^2\phi^2$  (red),  $V(\phi) = m_\phi^2f^2[1 + \cos(\phi/f)]$  (green), and  $V(\phi) = m_\phi^2f^2[\cosh(\phi/f) - 1]$  (blue). The constraints on the field mass are very similar for the three potentials, whereas the self-interaction parameter  $\lambda_\phi$  of the trigonometric potential remains unconstrained by the data.

$V_i(\phi_i) = m_{\phi_i}^2 f_i^2 [\cosh(\phi_i/f_i) - 1]$ . If there is no subscript, it means that it is the single field case.

First, in Fig. 6, we show the constraints for the single field cases, that is, the 1D marginalized posterior distribution of the free parameters for each model corresponding to the potentials  $V(\phi) = 1/2m_\phi^2\phi^2$ ,  $V(\phi) = m_\phi^2f^2[1 + \cos(\phi/f)]$ , and  $V(\phi) = m_\phi^2f^2[\cosh(\phi/f) - 1]$ . It can be noticed that the posteriors of the field masses are very similar for the three potentials, and that the observations considered can only put a lower bound on it, which is  $\log(m_\phi/\text{eV}) \gtrsim -21.9$  at 95% C.L. for the quadratic and hyperbolic cosine potentials and  $\log(m_\phi/\text{eV}) \gtrsim -21.8$  at 95% C.L. for the trigonometric cosine potential. In the case of the trigonometric potential, we see that its extra parameter  $\lambda_\phi$  appears unconstrained and the posterior looks practically the same as the prior we considered above for this parameter, which is consistent with previous studies

[26,36,37]. As for the hyperbolic cosine, we have already mentioned the close relationship between the field mass  $m_\phi$  and the self-interaction parameter  $\lambda_\phi$ , and then the constraints on the former are translated to  $\log(-\lambda_\phi) \gtrsim 3.6$  at 95% C.L. The excluded values of  $\lambda_\phi$  correspond to the cases in which SFDM has a significant contribution as an early radiation component. An example of this can be seen in Fig. 7.

For completeness, we also present in Fig. 8 the 1D posterior distributions for the cosmological common parameters of the models: the density parameters (SFDM and  $\Lambda$ ) and the Hubble constant  $H_0$ . The posteriors are very similar for the three models, which shows that one recovers the results of the standard  $\Lambda$ CDM model.

In Fig. 9 we show the posteriors for the combinations  $V(\phi_1) = 1/2m_{\phi_1}^2\phi_1^2$  with  $V(\phi_2) = 1/2m_{\phi_2}^2\phi_2^2$ ,  $V(\phi_1) = 1/2m_{\phi_1}^2\phi_1^2$  with  $V(\phi_2) = m_{\phi_2}^2f^2[1 + \cos(\phi_2/f)]$ , and

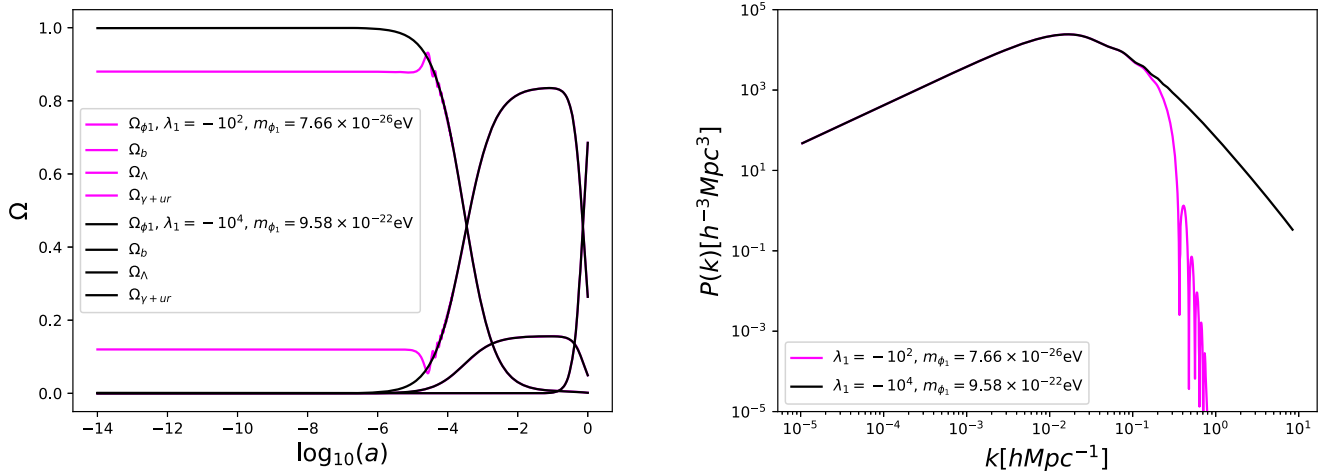


FIG. 7. Background and MPS evolution for the SFDM with potential  $V(\phi) = m_\phi^2f^2[\cosh(\phi/f) - 1]$ . Magenta lines correspond to  $\lambda_\phi = -10^2$  with  $m_\phi = 7.66 \times 10^{-26}$  eV, which are ruled out from the constraints obtained. We can see the scalar field contribution to radiation. On the other hand, black lines, that correspond to  $\lambda_\phi = -10^4$  with  $m_\phi = 9.58 \times 10^{-22}$  eV, represent values within the confidence regions.

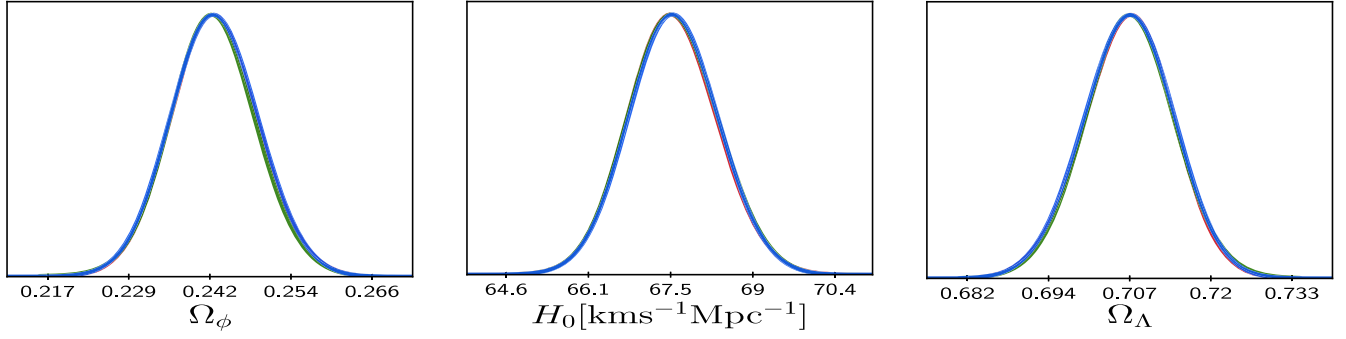
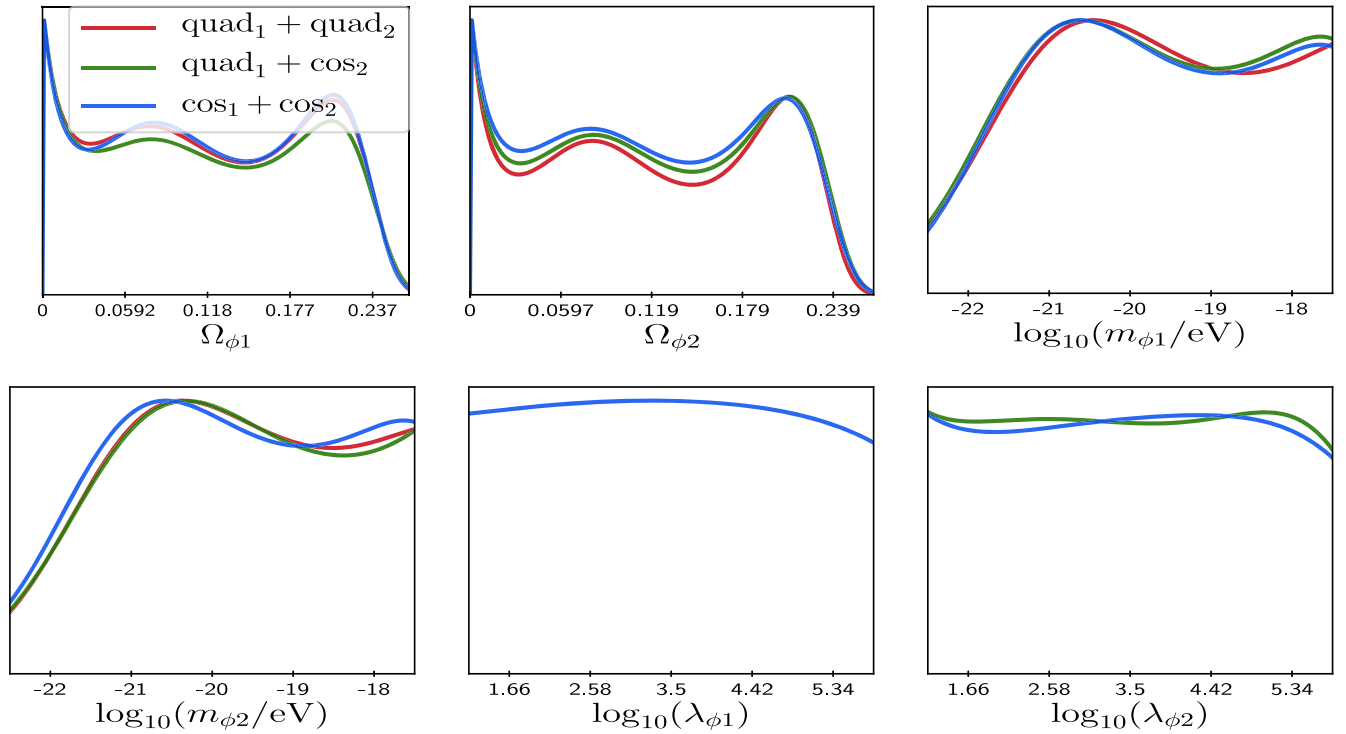


FIG. 8. 1D posterior distribution for the cosmological common parameters of all the models studied in this work.

FIG. 9. 1D posterior distribution for the two SFDM with the potentials  $V(\phi_{1,2}) = 1/2m_{\phi_{1,2}}^2\phi_{1,2}^2$  (red),  $V(\phi_1) = 1/2m_{\phi_1}^2\phi_1^2$  with  $V(\phi_2) = m_{\phi_2}^2 f^2 [1 + \cos(\phi_2/f)]$  (green), and  $V(\phi_{1,2}) = m_{\phi_{1,2}}^2 f^2 [1 + \cos(\phi_{1,2}/f)]$  (blue).

$V(\phi_{1,2}) = m_{\phi_{1,2}}^2 f^2 [1 + \cos(\phi_{1,2}/f)]$ . For the quadratic-quadratic and quadratic-cos combinations, we found a lower bound for the mass of both fields given by  $\log_{10}(m_{\phi_{1,2}}/\text{eV}) = -22.1$  at 95%. While, for the cos-cos combination, the lower bound for the mass of field one is  $\log_{10}(m_{\phi_1}/\text{eV}) = -22.1$  at 95% and for the second field  $\log_{10}(m_{\phi_2}/\text{eV}) = -22.2$  at 95%. We also found that the density parameter  $\Omega_{\phi_i}$  of one field depends on the  $\Omega_{\phi_j}$  of the other field. That is, if  $\Omega_{\phi_1}$  dominates then  $\Omega_{\phi_2}$  is small, and the other way around, because the total contribution remains constant. In [45] the authors propose two scalar fields (with the possibility of a third one) with masses  $m_{\phi_1} \approx 10^{-22}$  and  $m_{\phi_2} \approx 10^{-20}$  eV, and these values are

within our confidence regions. The fact that the lighter field dominates over the massive field is also in agreement with our results. The triangle plots of the MSFDM parameters in Figs. 6 and 9 can be seen in Appendix C.

As we have mentioned, the main objective is to present the model of multiple scalar fields as dark matter. Although, for completeness, we compute the Bayes factor  $\ln \mathcal{B}_{i,j}$  by using the numerical package MCEvidence [75], and the ratio is done with respect to CDM. The results are shown in Table I. Following the Jeffreys guideline [69], if  $\ln \mathcal{B}_{i,j} > 5$  we have a decisive strength against model  $i$ ; if  $5 > \ln \mathcal{B}_{i,j} > 2.5$  it means a strong strength; if  $2.5 > \ln \mathcal{B}_{i,j} > 1$  we have a significant strength, and if  $\ln \mathcal{B}_{i,j} < 1$  the data prefer

TABLE I. Bayes factor for SFDM and double SFDM with different potentials using  $\Lambda$ CDM as reference.

	Quad	Cosh	Quad <sub>1</sub> + quad <sub>2</sub>
$\ln \mathcal{B}_{i,\Lambda\text{CDM}}$	1.59	0.85	2.13

model  $i$ . In general, we should be careful taking the values of the Bayes factor since some of the parameters were unconstrained by the data [76]. On the other hand, the fact that the posteriors of the parameters of the scalar fields are not Gaussian prevents us from using other information criteria such as the Akaike information criterion, Bayesian information criterion, or the Bayesian complexity, since they need (or assume) the Gaussianity of the posterior. See, for example, [77,78]. On the other hand, we do not present the Bayes factor for the trigonometric potential cosine nor for the models with more than one field because the posteriors are not monomodal and some parameters are not constrained, which can cause the method used in MCEvidence to fail [75].

We found that the maximum of the likelihoods corresponds to the same value  $-\ln \mathcal{L}_{\max} = 523.03$ . That is, we can find a suitable combination of parameters such that the model in place resembles the behavior of a cold dark matter.

#### IV. CONCLUSIONS

In this paper, we presented the cosmological constraints of the multiscalar field dark matter model, in which we assume the dark matter is composed of different ultralight scalar fields. The idea was introduced to alleviate some of the cosmological and astrophysical discrepancies, for instance, the distinct values of the single scalar field mass obtained when considering different observations, where more than one field is needed in order to explain them. As a first approximation, we took for granted that the scalar fields are real, spatially homogeneous, and do not interact with each other. We presented the equations that describe the evolution of the background and perturbations for  $N$  scalar fields, and by using the polar change of variables we avoided the scalar field characteristic oscillations. Thus, we obtained a general expression for the fields' evolution that depends on the potential and its derivatives, in particular, the equations for the potentials  $V(\phi) = 1/2m_\phi^2\phi^2$ ,  $V(\phi) = m_\phi^2f^2[1 + \cos(\phi/f)]$ , and  $V(\phi) = m_\phi^2f^2[\cosh(\phi/f) - 1]$ . Under this change of variables, these three configurations are described by a single system of equations where the parameter  $\lambda_\phi$  is able to decide the type of potential to use.

We showed the evolution for the background, MPS, and the CMB power spectrum using a modified version of the CLASS code [21,25,63] with two dark matter components. We considered the following combinations: (a) cold dark matter and a scalar field with potential  $V(\phi) = 1/2m_\phi^2\phi^2$ ,

and two scalar field models, with (b) both potentials  $V(\phi) = 1/2m_\phi^2\phi^2$ , (c)  $V(\phi) = 1/2m_\phi^2\phi^2$  and  $V(\phi) = m_\phi^2f^2[1 + \cos(\phi/f)]$ , and (d)  $V(\phi) = 1/2m_\phi^2\phi^2$  and  $V(\phi) = m_\phi^2f^2[\cosh(\phi/f) - 1]$ . Since the fields are independent from each other, we introduced the parameter  $R$  to have the field one as reference. We showed that the evolution of the background is mainly affected at the beginning of the scalar fields' oscillations since its amplitude depends on the masses and the contribution that each one has to the total dark matter, being bounded by the heaviest and lightest masses; however, these do not depend on  $\lambda_\phi$ . After the oscillations have started, the fields' evolution only depend on  $\Omega_{\phi_i,0}$ . On the other hand, we found that, in all combinations, the MPS presents the characteristic cutoff of the single field at small scales. However, it does not present the oscillations of the single case due to the superposition of the different fields. This cutoff is far from the  $\Lambda$ CDM behavior when the lightest field dominates, and if the heaviest one dominates the MPS behavior approaches the  $\Lambda$ CDM model. For the case in which one of the fields has the axion potential, the characteristic bump appeared when it had a light mass with large  $\lambda_\phi$  values. On the contrary, if the mass is heavier, the bump disappeared regardless of the values of  $\lambda_\phi$  and  $R$ . On the other hand, in the CMB power spectrum, we have not found significant changes unless one of the fields has  $m_{\phi_i} \leq 10^{-26}$  eV. That is, regardless of the number of fields we can always find a combination of the fields that matches the CMB observations where the total contribution of dark matter is  $\Omega_{\text{DM}} = 0.264$ , given by Planck 18 data [55].

We performed the parameter inference analysis with the MONTE PYTHON code [67,68] using BAO, big bang nucleosynthesis, Ly- $\alpha$  forest, and supernovae for a single scalar field with the three potentials mentioned above and for double scalar fields. In the latter case, for simplicity we used the following combination of potentials:  $V(\phi_1) = 1/2m_{\phi_1}^2\phi_1^2$  with  $V(\phi_2) = 1/2m_{\phi_2}^2\phi_2^2$ ,  $V(\phi_1) = 1/2m_{\phi_1}^2\phi_1^2$  with  $V(\phi_2) = m_{\phi_2}^2f^2[1 + \cos(\phi_2/f)]$ , and  $V(\phi_1) = m_{\phi_1}^2f^2[1 + \cos(\phi_1/f)]$  with  $V(\phi_2) = m_{\phi_2}^2f^2[1 + \cos(\phi_2/f)]$ . For the single case, we found a bound for the mass values that corresponds to the one reported by the Ly- $\alpha$  data. We also presented the constrictions for the potential  $V(\phi) = m_\phi^2f^2[\cosh(\phi/f) - 1]$  where we have found a bound for  $\lambda_\phi$  and, therefore, for the scalar field mass, where the latter is also in agreement with the data reported by the Ly- $\alpha$ . In this case, the excluded values correspond to the cases in which the scalar field contributes to radiation as can be seen in Fig. 7. For the double field models, we found bounds for the masses and that the contribution of the fields depends on each other. Within our confidence regions are the masses reported in [45], in which more than one scalar field is needed to explain the observed galaxies' halos.

Finally, we have found that adding more scalar fields in order to explain astrophysical phenomena does not affect the known cosmology. So the MSFDM can be an alternative candidate to dark matter that is able to explain the observations at the cosmological and astrophysical levels. Its difference with other models is seen in the MPS at small scales. The results presented here can be generalized to a larger number of fields with different potentials. We expect that forthcoming observations of collaborations such as DESI and LSST will allow us to better constrain the parameters of our model.

### ACKNOWLEDGMENTS

The authors thank Luis Ureña for the long and productive discussions about the paper. L. O. T. T acknowledge financial support from a CONACyT doctoral fellowship. J. A. V. acknowledges the support provided by FOSEC SEP-CONACYT Investigación Básica A1-S-21925 and UNAM-DGAPA-PAPIIT IA104221. This work was partially supported by CONACyT México under Grants No. A1-S-8742, No. 304001, No. 376127, and No. 240512. The authors are grateful for the computing time granted by Laboratorio Nacional de Cómputo de Alto Desempeño and CONACYT in the Supercomputer Hybrid Cluster “Xihucotl” at General Coordination of Information and Communications Technologies (CGSTIC) of CINVESTAV and Abacus clusters at Cinvestav, IPN; I0101/131/07 C-234/07 of the Instituto Avanzado de Cosmología (IAC) Collaboration.

### APPENDIX A: COMPARISON WITH `axionCAMB`

In addition to CLASS, there is a code that solves the cosmology for an ultralight axion, this is a modification to the CAMB code [79,80] called `axionCAMB` [30,81]. For the case where only the scalar field is present, the formalism presented in this work and the results of `axionCAMB` [30] are in agreement as mentioned in [21]. Similarly, in [30], the authors also studied the combination of an ultralight axion with CDM. In Fig. 10, we have reproduced the right side of Fig. 2 of the same reference for  $R > 0.1$  and  $m_\phi = 10^{-27}$  eV. We found that the code presented here is in good agreement with the results of [30] except for small values of  $R$ , which translates to very small contributions from the scalar field ( $\Omega_\phi \sim < 0.02$ ).

### APPENDIX B: EXTENSIONS TO MSFDM MODEL: NEUTRINO MASSES AND CURVATURE

It is well known that neutrinos have effects on the evolution of the Universe [82,83], in particular, on the MPS [84] where the MSFDM model has differences with respect to  $\Lambda$ CDM. Therefore, in this section we vary the neutrino masses to see the effects on our model. We assume the neutrino model already presented in Sec. II A. In Fig. 11, we show the evolution of the linear matter power spectrum

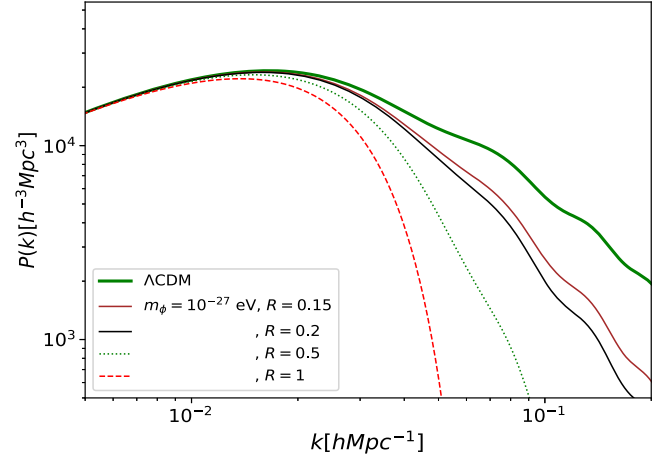


FIG. 10. Evolution of the linear matter power spectrum at  $z = 0$  for a CDM + SFDM model with  $V(\phi) = \frac{1}{2}m_\phi^2\phi^2$  with mass value  $m_\phi = 10^{-27}$  eV and  $R = 0.15, 0.2, 0.5,$  and  $1$ . Colors and line types were chosen to match Fig. 2 of [30] for an easy comparison.

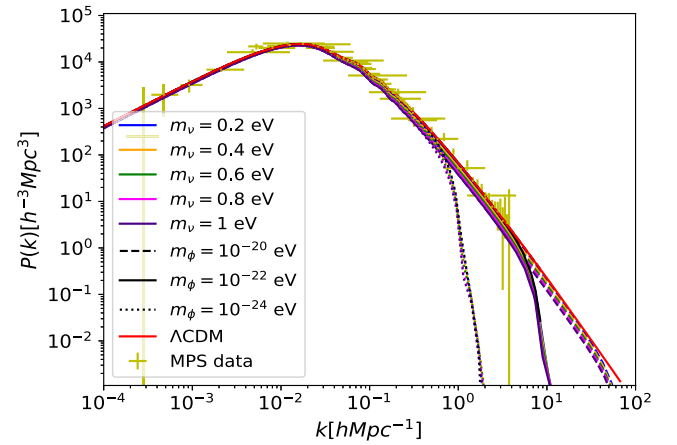


FIG. 11. Evolution of the linear matter power spectrum at  $z = 0$  for  $V(\phi) = \frac{1}{2}m_\phi^2\phi^2$  with neutrino masses  $m_\nu = 0.2, 0.4, 0.6, 0.8,$  and  $1$  eV. Colored dotted lines represent the combinations with  $m_\phi = 10^{-24}$  eV, colored solid lines with  $m_\phi = 10^{-22}$  eV, and colored dashed lines with  $m_\phi = 10^{-20}$  eV. For example, the blue dashed line represents a model with  $m_\nu = 0.2$  and  $m_\phi = 10^{-20}$  eV. The black lines represent the case for the SFDM with masses  $m_\phi = 10^{-24}$  eV (dotted),  $m_\phi = 10^{-22}$  eV (solid), and  $m_\phi = 10^{-20}$  eV (dashed) using the base model for neutrinos used in [55]. The solid red line represents the MPS for  $\Lambda$ CDM. The data points for the MPS are the same as used in Sec. II C and were obtained from [65].

for the SFDM model (one field) with the potential  $V(\phi) = \frac{1}{2}m_\phi^2\phi^2$  with mass values  $m_\phi = 10^{-24}, 10^{-22},$  and  $10^{-20}$  eV each combined with neutrino masses  $m_\nu = 0.2, 0.4, 0.6, 0.8,$  and  $1$  eV; bigger values are already discarded [85–88]. We found no significant differences with respect to the neutrino base model. However, there could be degeneracies

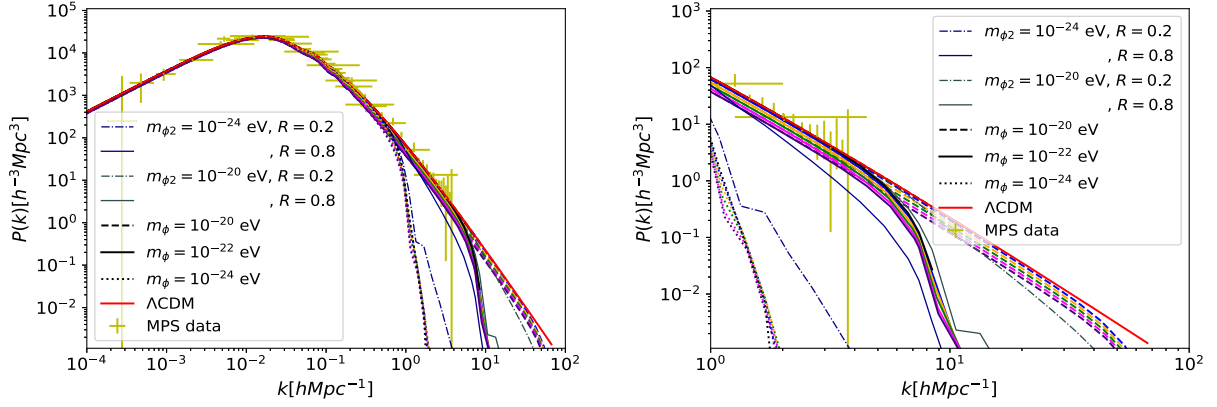


FIG. 12. Evolution of the linear matter power spectrum at  $z = 0$  for a single field with potential  $V(\phi) = \frac{1}{2}m_\phi^2\phi^2$  with neutrino masses  $m_\nu = 0.2$  (blue),  $0.4$  (orange),  $0.6$  (green),  $0.8$  (magenta), and  $1$  eV (indigo) compared with the double field model with  $V(\phi_{1,2}) = \frac{1}{2}m_{\phi_{1,2}}^2\phi_{1,2}^2$  using  $m_{\phi_1} = 10^{-22}$  eV and different values of  $m_{\phi_2}$  and  $R$ . For the single case varying neutrino mass, colored dotted lines represent the combinations with  $m_\phi = 10^{-24}$  eV, colored solid lines with  $m_\phi = 10^{-22}$  eV, and colored dashed lines with  $m_\phi = 10^{-20}$  eV. The dark blue and gray lines represent the MSFDM evolution and the solid red line represents the MPS for  $\Lambda$ CDM. The data points for the MPS are the same as used in Sec. II C and were obtained from [65]. On the right side, a small-scale enlargement is shown where you can see the consequence of changing the values of the neutrino masses and the scalar fields.

with the MSFDM. For example, in Fig. 12 we compare the evolution of the MPS for the double field model, with potentials  $V(\phi_{1,2}) = \frac{1}{2}m_{\phi_{1,2}}^2\phi_{1,2}^2$ , and the single field case with different neutrino masses shown in Fig. 11. For the double field model, we fix the mass value of field one to  $m_{\phi_1} = 10^{-22}$  eV while the second mass takes  $m_{\phi_2} = 10^{-24}$  and  $10^{-20}$  eV, with  $R = 0.2$  and  $R = 0.8$ . We can see that the MPS of both models are very similar.

In the same way, we study the case where we add curvature to the scalar field model and find similar results as for  $\Lambda$ CDM. This can be seen in the left panel of Fig. 14 where we show the 1D posterior for  $\Omega_k$ .

### APPENDIX C: MSFDM: TRIANGLE PLOTS

In this appendix, we show the triangle plots for the different potential combinations analyzed in Sec. II C. In Fig. 13, we show the posteriors of the physical baryon density parameter  $\omega_{b,0}$ , the logarithmic power spectrum scalar amplitude  $\log(10^{10}A_s)$ , the scalar spectral index  $n_s$ , the Thomson scattering optical depth due to reionization  $\tau_{\text{reio}}$ , the Hubble constant  $H_0$  in  $\text{km s}^{-1} \text{Mpc}^{-1}$ , the scalar field mass  $\log_{10}(m_{\phi_i}/\text{eV})$ , the dark energy density parameter  $\Omega_\Lambda$ , and the dark matter density parameter  $\Omega_{\text{DM}}$ . The last one refers to cold dark matter for  $\Lambda$ CDM and to the scalar field for SFDM using Planck 18 data [55,89], the 3D matter power spectrum inferred from Lyman- $\alpha$  data from BOSS and eBOSS Collaborations [65], the Ly- $\alpha$  BAO from eBOSS DR14 [70], the Galaxy BAO from DR12 [71], 6dFGS [72], and SDSS DR7 [73], and the SNe Ia survey Pantheon [74]. As we can see, there are no differences between the constrictions of the  $\Lambda$ CDM and SFDM parameters and they agree with the values reported in

[55]. Thus, in Sec. III A we decided to vary only the parameters corresponding to the scalar fields, leaving the rest of the parameters fixed. Using the fact that the SFDM model provides similar constraints for the basic parameters using the Planck data and given that we found similar restrictions for the scalar field mass with and without Planck 18 data, we decided to use only the MPS from Ly- $\alpha$ , BAO, and SNe Ia data. This change in the dataset used also gives us a reduction in computational time.

On the other hand, in Figs. 15–20 we also show the 1D and 2D posteriors of the combinations studied in Sec. III A when we consider each dataset separately. In all cases, we find that we need to combine the datasets to improve the constraints on the parameters of the scalar fields. Note that, by using only the BAO data, the restriction for  $H_0$  gives high values compared to Planck 18, so it is necessary to use more datasets in order to constrain this parameter (see [70]).

### APPENDIX D: A GENERAL PARAMETRIZATION

In [90,91] the authors proposed a general parametrization, called  $\alpha, \beta, \gamma$  parametrization, to describe the transfer function of non-CDM (nCDM) models, in particular, the fuzzy dark matter model, which in our case corresponds to a single SFDM with the quadratic potential. In their studies, they found that models allowed correspond those that meet  $m_\phi \gtrsim 10^{-22}$  eV. We found this parametrization could also describe the combination of two fields with different combinations of potentials with the possible exception of the cases in which the characteristic bump of the trigonometric cosine-type potential occurs. In Fig. 21, we show some examples of the transfer function for the combinations SFDM + CDM, quad<sub>1</sub> + quad<sub>2</sub>, quad<sub>1</sub> + cos<sub>2</sub>, and

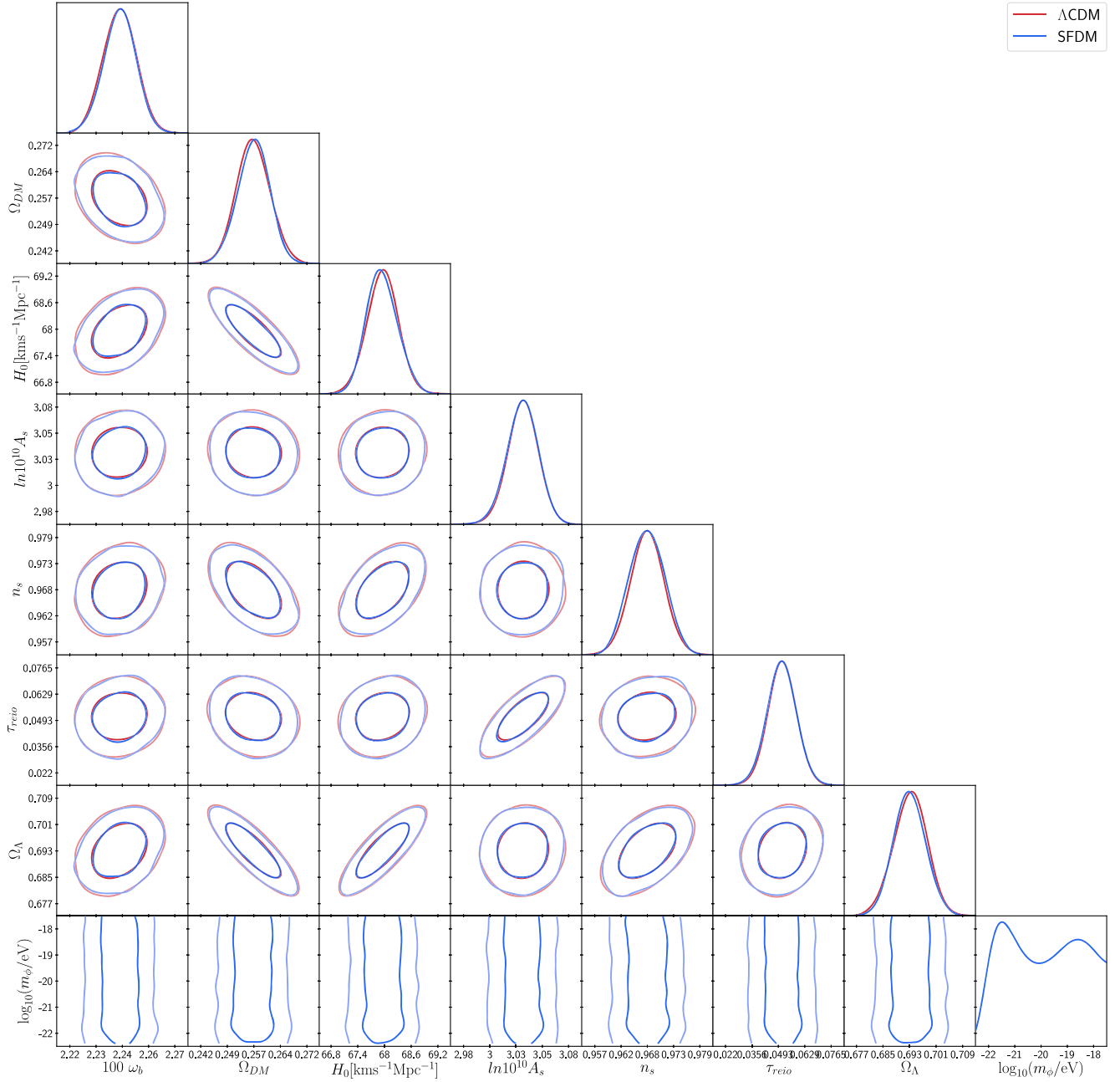


FIG. 13. Triangle plots for the SFDM with potential  $V(\phi) = \frac{1}{2} m_\phi^2 \phi^2$  compared with  $\Lambda$ CDM as reference using the data from Planck 18, MPS from Ly- $\alpha$  BAO and SNe Ia. See text for details.

quad<sub>1</sub> + cos  $h_2$  (solid lines) and the transfer function with the  $\alpha, \beta, \gamma$  parametrization (dashed lines). Although the values of the parameters  $\alpha, \beta,$  and  $\gamma$  were set by hand, we can see they resemble the numerical results we obtained with the exception of the cosine potential, where the characteristic

bump cannot be described by this parametrization. However, further studies similar to the one done in [92] are necessary to determine the relationship between the properties of the scalar fields and the  $\alpha, \beta,$  and  $\gamma$  parameters and to obtain the respective constraints.

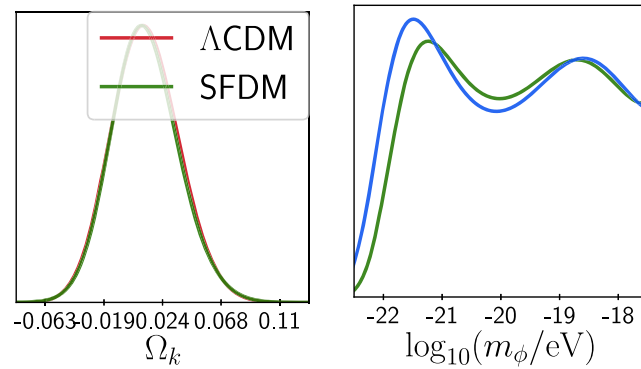


FIG. 14. On the left, we show the constraints on the curvature parameter for  $\Lambda$ CDM and for the SFDM model. On the right, we show the mass value constriction for the SFDM model with potential  $V(\phi) = \frac{1}{2}m_\phi^2\phi^2$  using the data from Planck 18, MPS from Ly- $\alpha$ , BAO, and SNe Ia (blue), and MPS from Ly- $\alpha$ , BAO, and SNe Ia (green).

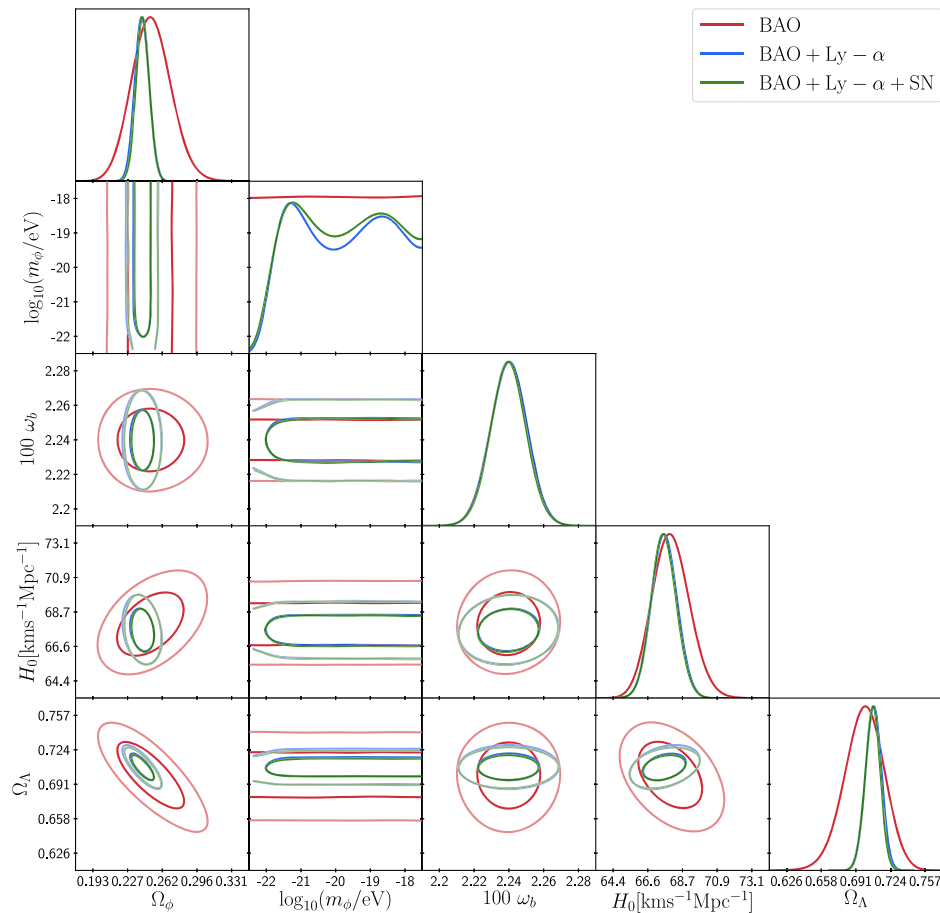


FIG. 15. 1D and 2D posterior distribution for the potential  $V(\phi) = \frac{1}{2}m_\phi^2\phi^2$ . We found constrictions for  $m_\phi$  and  $\Omega_\phi$ . We see that it is necessary to use different datasets to constrain the parameters of the scalar field. Here and in the following figures, the Ly- $\alpha$  label refers to the MPS inferred from these data. See the text for details.

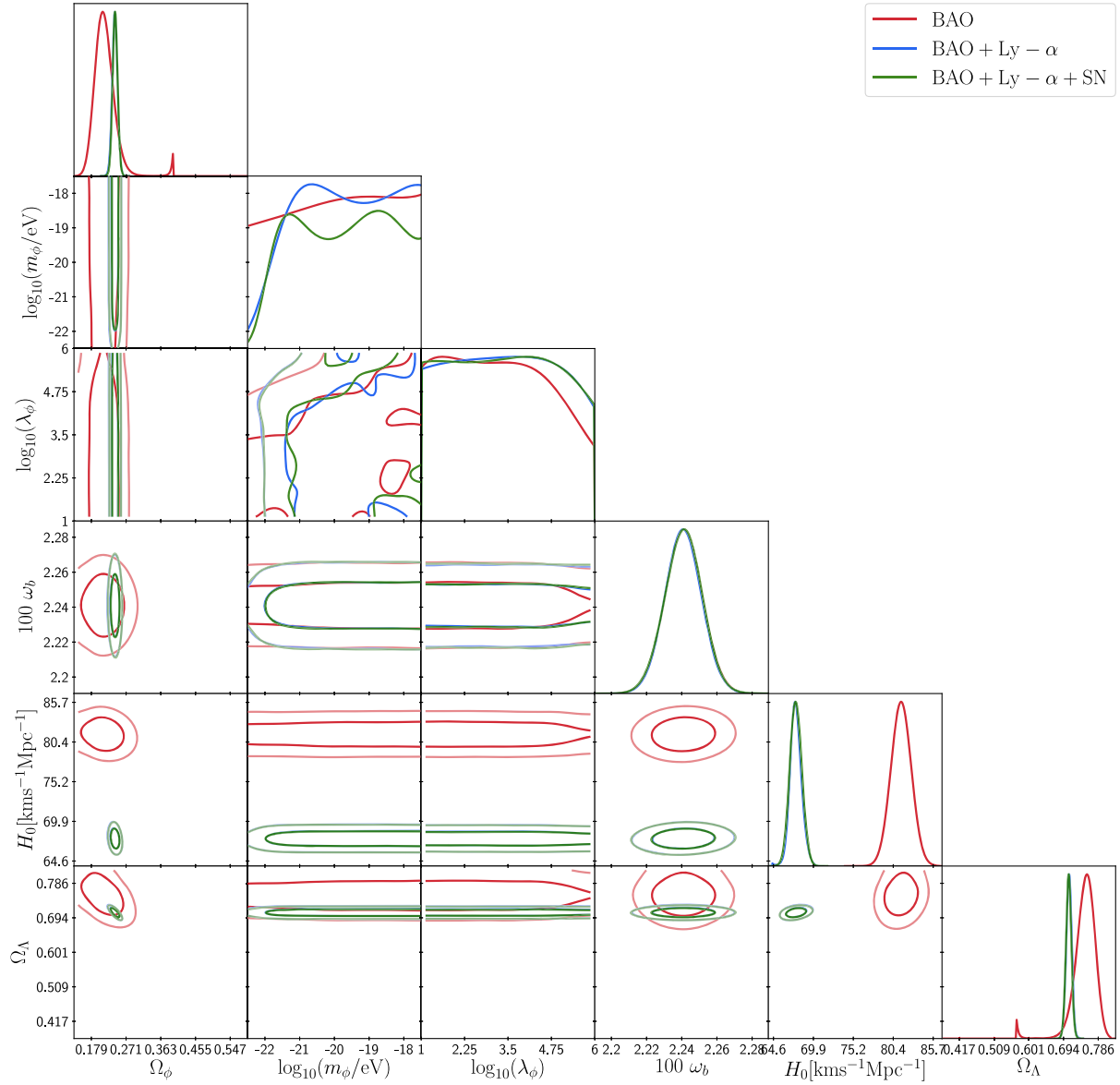


FIG. 16. 1D and 2D posterior distribution for the potential  $V(\phi) = m_\phi^2 f^2 [1 + \cos(\phi/f)]$ . We found constrictions only for  $m_\phi$  and  $\Omega_\phi$ . It is necessary to use different datasets to constrain the parameters of the scalar field.

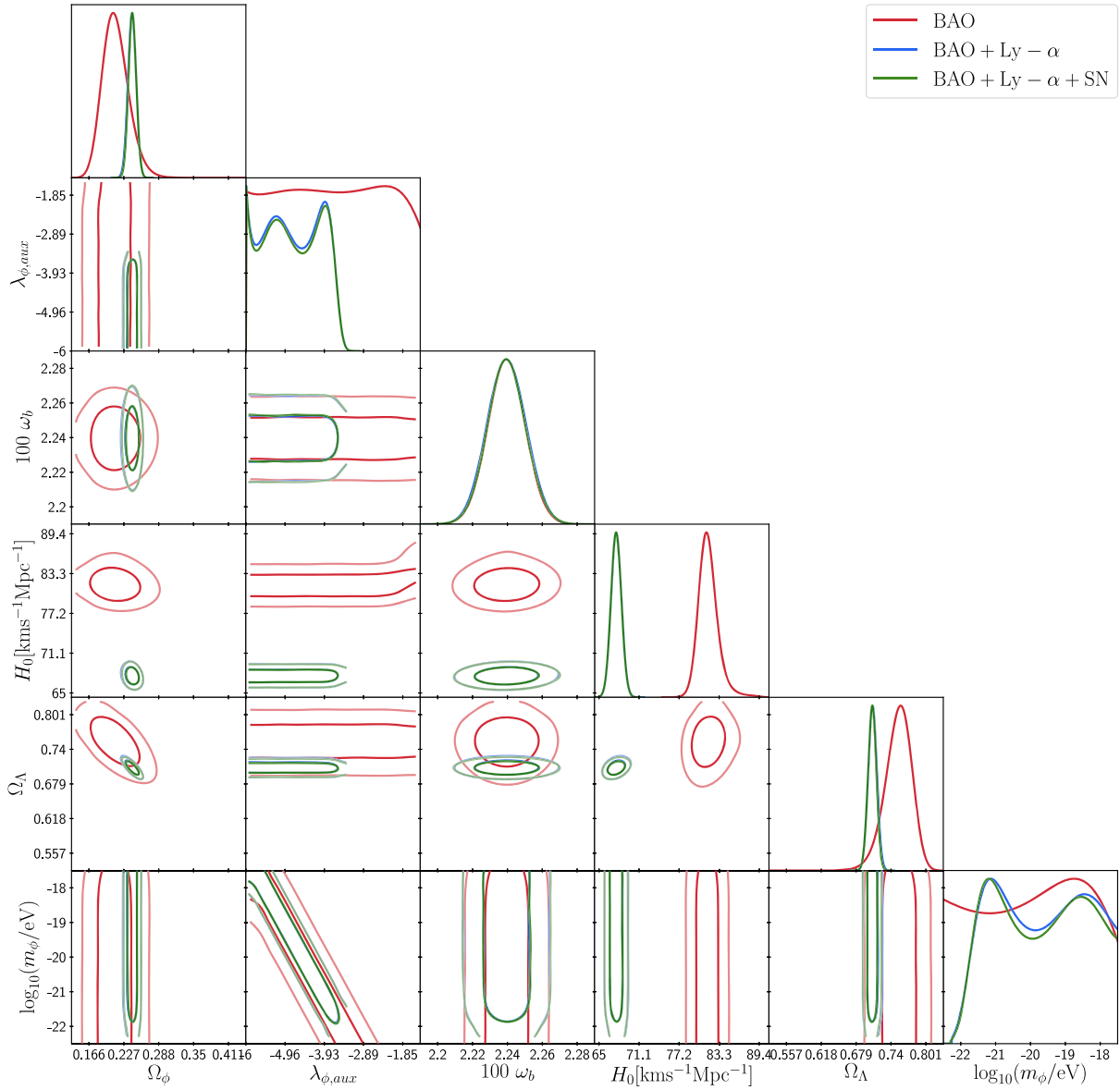


FIG. 17. 1D and 2D posterior distribution for  $V(\phi) = m_\phi^2 f^2 [\cosh(\phi/f) - 1]$ .

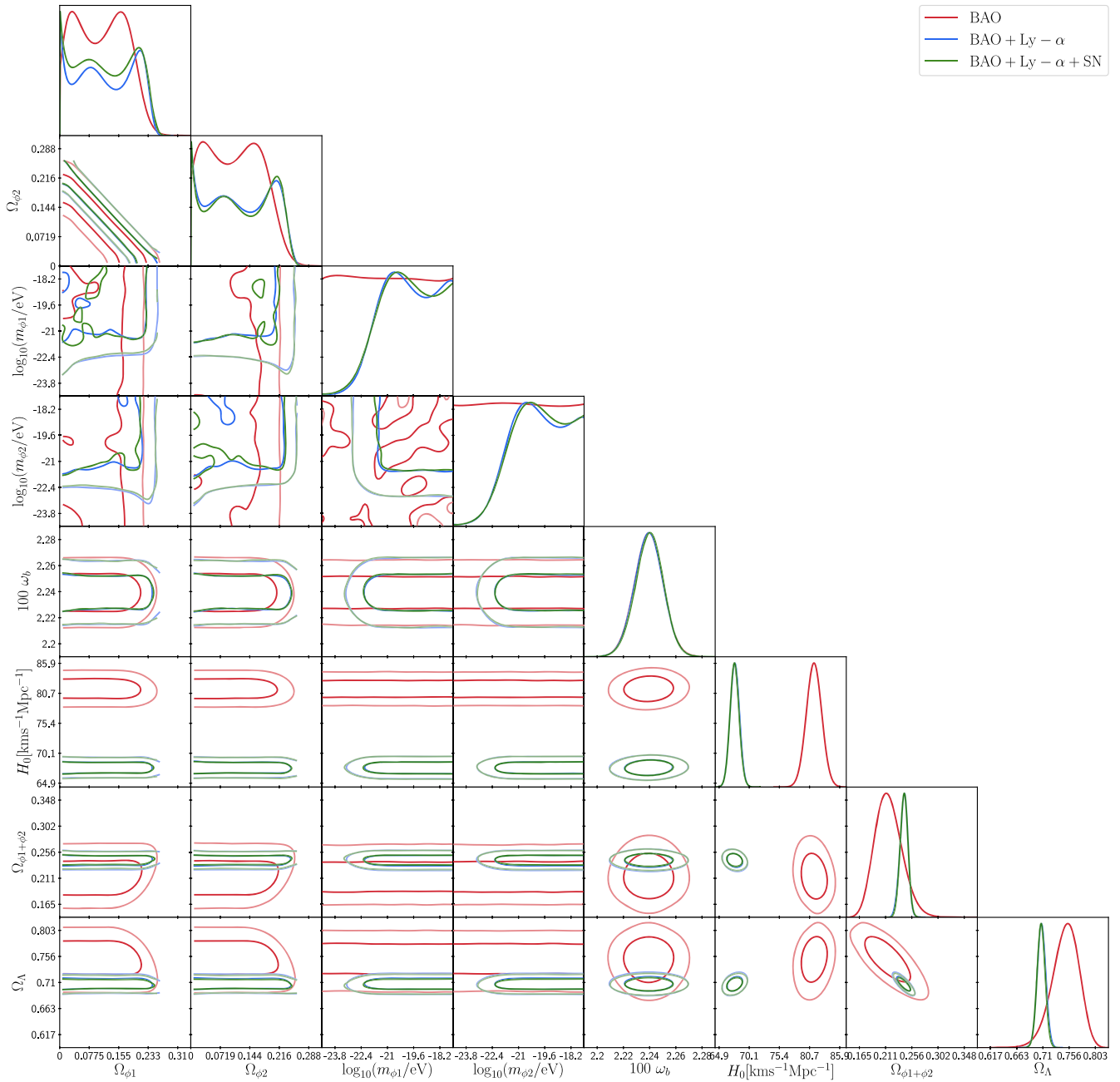


FIG. 18. 1D and 2D posterior distribution of the fields considering potential  $V(\phi_1) = 1/2m_{\phi_1}^2\phi_1^2$  for the first field with  $V(\phi_2) = 1/2m_{\phi_2}^2\phi_2^2$ .

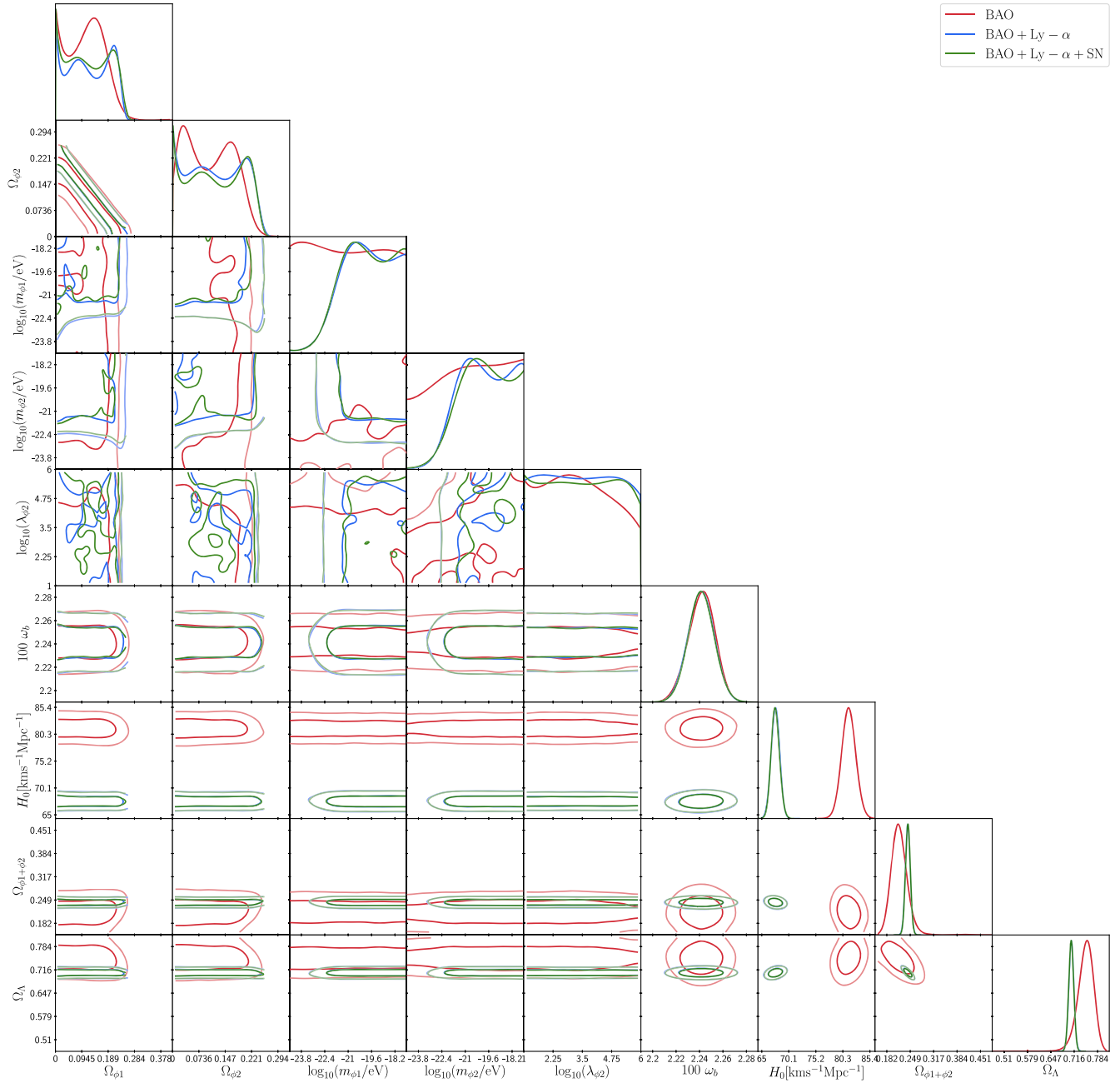


FIG. 19. 1D and 2D posterior distribution of the fields considering potential  $V(\phi_1) = 1/2m_{\phi_1}^2\phi_1^2$  for the first field with  $V(\phi_2) = m_{\phi_2}^2f^2[1 + \cos(\phi_2/f)]$ .

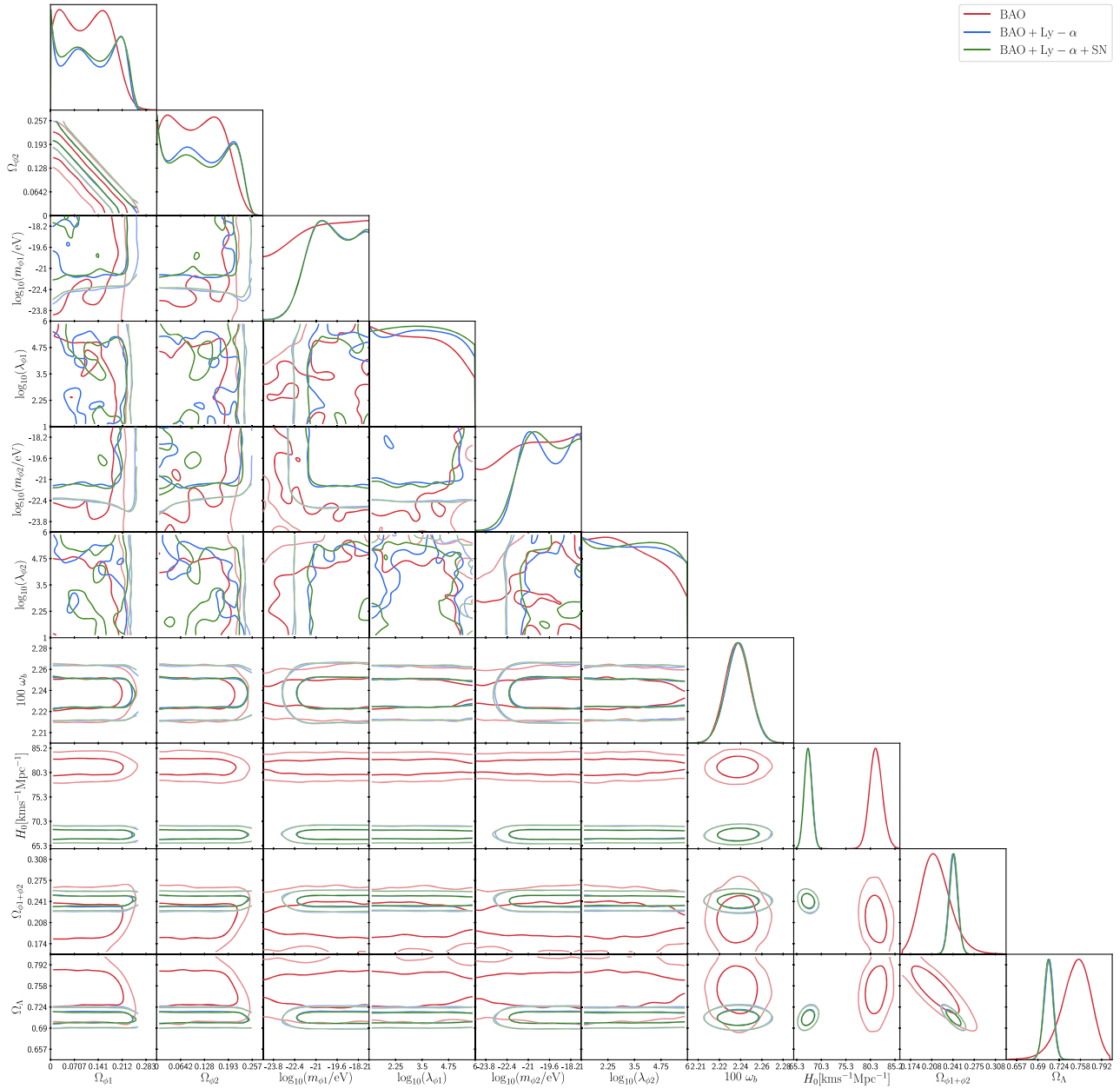


FIG. 20. 1D and 2D posterior distribution of the fields when both have the potential  $V(\phi) = m_\phi^2 f^2 [1 + \cos(\phi/f)]$ .

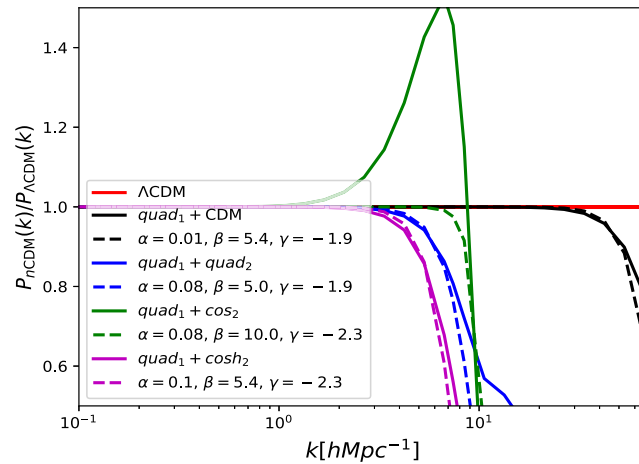


FIG. 21. Transfer functions for the combinations SFDM + CDM with  $m_\phi = 10^{-20}$  eV and  $R = 0.2$  (black solid line);  $quad_1 + quad_2$  with  $m_{\phi_1} = 10^{-22}$  eV,  $m_{\phi_2} = 10^{-20}$  eV, and  $R = 0.2$  (blue solid line);  $quad_1 + cos_2$  with  $m_{\phi_1} = 10^{-22}$  eV,  $m_{\phi_2} = 10^{-22}$  eV,  $\lambda_{\phi_2} = 10^5$ , and  $R = 0.2$  (green solid line); and  $quad_1 + cos h_2$  with  $m_{\phi_1} = 10^{-22}$  eV,  $m_{\phi_2} = 0.3 \times 10^{-18}$  eV,  $\lambda_{\phi_2} = -4 \times 10^5$ , and  $R = 0.5$ . The dashed lines correspond to the transfer function using the  $\alpha$ ,  $\beta$ ,  $\gamma$  parametrization for different combinations of  $\alpha$ ,  $\beta$ , and  $\gamma$ .

- [1] D. H. Weinberg, J. S. Bullock, F. Governato, R. Kuzio de Naray, and A. H. G. Peter, Cold dark matter: Controversies on small scales, *Proc. Natl. Acad. Sci. U.S.A.* **112**, 12249 (2015).
- [2] P. Bull *et al.*, Beyond  $\Lambda$ CDM: Problems, solutions, and the road ahead, *Phys. Dark Universe* **12**, 56 (2016).
- [3] S. Y. Kim, A. H. G. Peter, and J. R. Hargis, Missing Satellites Problem: Completeness Corrections to the Number of Satellite Galaxies in the Milky Way are Consistent with Cold Dark Matter Predictions, *Phys. Rev. Lett.* **121**, 211302 (2018).
- [4] DES Collaboration, Milky Way Satellite Census. III. Constraints on Dark Matter Properties from Observations of Milky Way Satellite Galaxies, *Phys. Rev. Lett.* **126**, 091101 (2021).
- [5] S.-J. Sin, Late-time phase transition and the galactic halo as a Bose liquid, *Phys. Rev. D* **50**, 3650 (1994).
- [6] J.-w. Lee and I.-g. Koh, Galactic halos as boson stars, *Phys. Rev. D* **53**, 2236 (1996).
- [7] F. Guzmán, T. Matos, and H. Villegas, Scalar fields as dark matter in spiral galaxies: Comparison with experiments, *Astron. Nachr.* **320**, 97 (1999).
- [8] T. Matos and F. S. Guzman, Scalar fields as dark matter in spiral galaxies, *Classical Quantum Gravity* **17**, L9 (2000).
- [9] W. Hu, R. Barkana, and A. Gruzinov, Cold and Fuzzy Dark Matter, *Phys. Rev. Lett.* **85**, 1158 (2000).
- [10] C. G. Boehmer and T. Harko, Can dark matter be a Bose-Einstein condensate?, *J. Cosmol. Astropart. Phys.* **06** (2007) 025.
- [11] L. Hui, J. P. Ostriker, S. Tremaine, and E. Witten, Ultralight scalars as cosmological dark matter, *Phys. Rev. D* **95**, 043541 (2017).
- [12] J. Magaña and T. Matos, A brief review of the scalar field dark matter model, *J. Phys. Conf. Ser.* **378**, 012012 (2012).
- [13] T. Matos, A. Vazquez-Gonzalez, and J. Magana,  $\phi^2$  as dark matter, *Mon. Not. R. Astron. Soc.* **393**, 1359 (2009).
- [14] A. Suárez, V. H. Robles, and T. Matos, A review on the scalar field/Bose-Einstein condensate dark matter model, in *Accelerated Cosmic Expansion*, edited by C. Moreno González, J. Madriz Aguilar, and L. Reyes Barrera, *Astrophysics and Space Science Proceedings Vol. 38* (Springer, Cham, 2014), pp. 107–142, [10.1007/978-3-319-02063-1\\_9](https://doi.org/10.1007/978-3-319-02063-1_9).
- [15] L. A. Ureña López, Brief review on scalar field dark matter models, *Front. Astron. Space Sci.* **6**, 47 (2019).
- [16] L. E. Padilla, J. A. Vázquez, T. Matos, and G. Germán, Scalar field dark matter spectator during inflation: The effect of self-interaction, *J. Cosmol. Astropart. Phys.* **05** (2019) 056.
- [17] V. H. Robles and T. Matos, Exact solution to finite temperature SFDM: Natural cores without feedback, *Astrophys. J.* **763**, 19 (2013).
- [18] A. Hernández-Almada and M. A. García-Aspeitia, Multi-state scalar field dark matter and its correlation with galactic properties, *Int. J. Mod. Phys. D* **27**, 1850031 (2017).
- [19] A. Navarro-Boullosa, A. Bernal-Bautista, and J. Vazquez, Bayesian analysis for rotational curves with  $\ell$ -boson stars as a dark matter component (to be published).
- [20] T. Matos, A. Vazquez-Gonzalez, and J. Magana, Study of several potentials as scalar field dark matter candidates, *AIP Conf. Proc.* **1083**, 144 (2008).
- [21] L. A. Ureña López and A. X. Gonzalez-Morales, Towards accurate cosmological predictions for rapidly oscillating scalar fields as dark matter, *J. Cosmol. Astropart. Phys.* **07** (2016) 048.

- [22] B. Li, T. Rindler-Daller, and P. R. Shapiro, Cosmological constraints on Bose-Einstein-condensed scalar field dark matter, *Phys. Rev. D* **89**, 083536 (2014).
- [23] A. Suárez and P.-H. Chavanis, Hydrodynamic representation of the Klein-Gordon-Einstein equations in the weak field limit: General formalism and perturbations analysis, *Phys. Rev. D* **92**, 023510 (2015).
- [24] A. Suárez and P.-H. Chavanis, Cosmological evolution of a complex scalar field with repulsive or attractive self-interaction, *Phys. Rev. D* **95**, 063515 (2017).
- [25] F. X. L. Cedeño, A. X. González-Morales, and L. A. Ureña López, Cosmological signatures of ultralight dark matter with an axionlike potential, *Phys. Rev. D* **96**, 061301 (2017).
- [26] F. X. Linares Cedeño, A. X. González-Morales, and L. A. Ureña López, Ultralight DM bosons with an axion-like potential: Scale-dependent constraints revisited, *J. Cosmol. Astropart. Phys.* **01** (2021) 051.
- [27] G. G. Ross, G. German, and J. A. Vázquez, Hybrid natural inflation, *J. High Energy Phys.* **05** (2016) 010.
- [28] T. Matos, J.-R. Luévano, I. Quiros, L. A. Ureña-López, and J. A. Vázquez, Dynamics of scalar field dark matter with a cosh-like potential, *Phys. Rev. D* **80**, 123521 (2009).
- [29] L. A. Ureña López, Scalar field dark matter with a cosh potential, revisited, *J. Cosmol. Astropart. Phys.* **06** (2019) 009.
- [30] R. Hlozek, D. Grin, D. J. E. Marsh, and P. G. Ferreira, A search for ultralight axions using precision cosmological data, *Phys. Rev. D* **91**, 103512 (2015).
- [31] A. Paredes and H. Michinel, Interference of dark matter solitons and galactic offsets, *Phys. Dark Universe* **12**, 50 (2016).
- [32] A. X. González-Morales, D. J. E. Marsh, J. Peñarrubia, and L. A. Ureña López, Unbiased constraints on ultralight axion mass from dwarf spheroidal galaxies, *Mon. Not. R. Astron. Soc.* **472**, 1346 (2017).
- [33] V. Lora, J. Magana, A. Bernal, F. J. Sanchez-Salcedo, and E. K. Grebel, On the mass of ultralight bosonic dark matter from galactic dynamics, *J. Cosmol. Astropart. Phys.* **02** (2012) 011.
- [34] E. Calabrese and D. N. Spergel, Ultra-light dark matter in ultra-faint dwarf galaxies, *Mon. Not. R. Astron. Soc.* **460**, 4397 (2016).
- [35] A. Sarkar, R. Mondal, S. Das, S. K. Sethi, S. Bharadwaj, and D. J. E. Marsh, The effects of the small-scale DM power on the cosmological neutral hydrogen (HI) distribution at high redshifts, *J. Cosmol. Astropart. Phys.* **04** (2016) 012.
- [36] E. Armengaud, N. Palanque-Delabrouille, C. Yèche, D. J. E. Marsh, and J. Baur, Constraining the mass of light bosonic dark matter using SDSS Lyman- $\alpha$  forest, *Mon. Not. R. Astron. Soc.* **471**, 4606 (2017).
- [37] V. Iršič, M. Viel, M. G. Haehnelt, J. S. Bolton, and G. D. Becker, First Constraints on Fuzzy Dark Matter from Lyman- $\alpha$  Forest Data and Hydrodynamical Simulations, *Phys. Rev. Lett.* **119**, 031302 (2017).
- [38] D. J. E. Marsh, Axion cosmology, *Phys. Rep.* **643**, 1 (2016).
- [39] P. Mocz *et al.*, First Star-Forming Structures in Fuzzy Cosmic Filaments, *Phys. Rev. Lett.* **123**, 141301 (2019).
- [40] O. Müller, M. S. Pawłowski, H. Jerjen, and F. Lelli, A whirling plane of satellite galaxies around Centaurus A challenges cold dark matter cosmology, *Science* **359**, 534 (2018).
- [41] L. E. Strigari, J. S. Bullock, M. Kaplinghat, J. D. Simon, M. Geha, B. Willman, and M. G. Walker, A common mass scale for satellite galaxies of the Milky Way, *Nature (London)* **454**, 1096 (2008).
- [42] I. J. Allali, M. P. Hertzberg, and F. Rompineve, Dark sector to restore cosmological concordance, *Phys. Rev. D* **104**, L081303 (2021).
- [43] K. Blum and L. Teodori, Gravitational lensing H0 tension from ultralight axion galactic cores, *Phys. Rev. D* **104**, 123011 (2021).
- [44] A. Arvanitaki, S. Dimopoulos, S. Dubovsky, N. Kaloper, and J. March-Russell, String axiverse, *Phys. Rev. D* **81**, 123530 (2010).
- [45] H. N. Luu, S. H. H. Tye, and T. Broadhurst, Multiple ultralight axionic wave dark matter and astronomical structures, *Phys. Dark Universe* **30**, 100636 (2020).
- [46] A. Paliathanasis and M. Tsamparlis, Two scalar field cosmology: Conservation laws and exact solutions, *Phys. Rev. D* **90**, 043529 (2014).
- [47] J. A. Vázquez, D. Tamayo, A. A. Sen, and I. Quiros, Bayesian model selection on scalar  $\epsilon$ -field dark energy, *Phys. Rev. D* **103**, 043506 (2021).
- [48] D. Benisty and E. I. Guendelman, Two scalar fields inflation from scale-invariant gravity with modified measure, *Classical Quantum Gravity* **36**, 095001 (2019).
- [49] K. Bamba, S. D. Odintsov, and P. V. Tretyakov, Inflation in a conformally-invariant two-scalar-field theory with an extra  $R^2$  term, *Eur. Phys. J. C* **75**, 344 (2015).
- [50] J. A. Vázquez, L. E. Padilla, and T. Matos, Inflationary cosmology: From theory to observations, *Rev. Mex. Fis. E* **17**, 73 (2020).
- [51] O. Bertolami, P. Carrilho, and J. Paramos, Two-scalar-field model for the interaction of dark energy and dark matter, *Phys. Rev. D* **86**, 103522 (2012).
- [52] V. M. Mehta, M. Demirtas, C. Long, D. J. E. Marsh, L. McAllister, and M. J. Stott, Superradiance in string theory, *J. Cosmol. Astropart. Phys.* **07** (2021) 033.
- [53] M. Cicoli, V. Guidetti, N. Righi, and A. Westphal, Fuzzy dark matter candidates from string theory, *J. High Energy Phys.* **05** (2022) 107.
- [54] E. Gutiérrez-Luna, B. Carvente, V. Jaramillo, J. Barranco, C. Escamilla-Rivera, C. Espinoza, M. Mondragón, and D. Núñez, Scalar field dark matter with two components: Combined approach from particle physics and cosmology, *Phys. Rev. D* **105**, 083533 (2022).
- [55] Planck Collaboration, Planck 2018 results. VI. Cosmological parameters, *Astron. Astrophys.* **641**, A6 (2020).
- [56] NO $\nu$ A Collaboration, Constraints on Oscillation Parameters from  $\nu_e$  Appearance and  $\nu_\mu$  Disappearance in NO $\nu$ A, *Phys. Rev. Lett.* **118**, 231801 (2017).
- [57] P. F. de Salas, D. V. Forero, C. A. Ternes, M. Tortola, and J. W. F. Valle, Status of neutrino oscillations 2018:  $3\sigma$  hint for normal mass ordering and improved  $CP$  sensitivity, *Phys. Lett. B* **782**, 633 (2018).
- [58] Super-Kamiokande Collaboration, Atmospheric neutrino oscillation analysis with external constraints in Super-Kamiokande I-IV, *Phys. Rev. D* **97**, 072001 (2018).
- [59] F. Capozzi, E. Lisi, A. Marrone, and A. Palazzo, Current unknowns in the three neutrino framework, *Prog. Part. Nucl. Phys.* **102** (2018) 48.

- [60] L. A. Ureña López, New perturbative method for analytical solutions in single-field models of inflation, *Phys. Rev. D* **94**, 063532 (2016).
- [61] T. Cookmeyer, J. Cookmeyer, D. Grin, and T. L. Smith, How sound are our ultralight axion approximations?, *Phys. Rev. D* **101**, 023501 (2020).
- [62] S. Passaglia and W. Hu, Accurate effective fluid approximation for ultralight axions, *Phys. Rev. D* **105**, 123529 (2022).
- [63] D. Blas, J. Lesgourgues, and T. Tram, The cosmic linear anisotropy solving system (class). Part II: Approximation schemes, *J. Cosmol. Astropart. Phys.* **07** (2011) 034.
- [64] [https://github.com/losvaldote/two\\_sfdm\\_class](https://github.com/losvaldote/two_sfdm_class).
- [65] S. Chabanier, M. Millea, and N. Palanque-Delabrouille, Matter power spectrum: From Ly $\alpha$  forest to CMB scales, *Mon. Not. R. Astron. Soc.* **489**, 2247 (2019).
- [66] <http://pla.esac.esa.int/pla/#home>.
- [67] T. Brinckmann and J. Lesgourgues, MontePython 3: Boosted MCMC sampler and other features, *Phys. Dark Universe* **24**, 100260 (2019).
- [68] B. Audren, J. Lesgourgues, K. Benabed, and S. Prunet, Conservative constraints on early cosmology with MONTEPYTHON, *J. Cosmol. Astropart. Phys.* **02** (2013) 001.
- [69] L. E. Padilla, L. O. Tellez, L. A. Escamilla, and J. A. Vazquez, Cosmological parameter inference with Bayesian statistics, *Universe* **7**, 213 (2021).
- [70] A. Cuceu, J. Farr, P. Lemos, and A. Font-Ribera, Baryon Acoustic Oscillations and the Hubble Constant: Past, Present and Future, *J. Cosmol. Astropart. Phys.* **10** (2019) 044.
- [71] BOSS collaboration, The clustering of galaxies in the completed SDSS-III Baryon Oscillation Spectroscopic Survey: Cosmological analysis of the DR12 galaxy sample, *Mon. Not. R. Astron. Soc.* **470**, 2617 (2017).
- [72] F. Beutler, C. Blake, M. Colless, D. H. Jones, L. Staveley-Smith, L. Campbell, Q. Parker, W. Saunders, and F. Watson, The 6df galaxy survey: Baryon acoustic oscillations and the local Hubble constant, *Mon. Not. R. Astron. Soc.* **416**, 3017 (2011).
- [73] A. J. Ross, L. Samushia, C. Howlett, W. J. Percival, A. Burden, and M. Manera, The clustering of the SDSS DR7 main Galaxy sample—I. A 4 per cent distance measure at  $z = 0.15$ , *Mon. Not. R. Astron. Soc.* **449**, 835 (2015).
- [74] D. M. Scolnic *et al.*, The complete light-curve sample of spectroscopically confirmed SNe Ia from Pan-STARRS1 and cosmological constraints from the combined Pantheon sample, *Astrophys. J.* **859**, 101 (2018).
- [75] A. Heavens, Y. Fantaye, A. Mootoovaloo, H. Eggers, Z. Hosenie, S. Kroon *et al.*, Marginal likelihoods from Monte Carlo Markov chains, [arXiv:1704.03472](https://arxiv.org/abs/1704.03472).
- [76] R. Trotta, Bayes in the sky: Bayesian inference and model selection in cosmology, *Contemp. Phys.* **49**, 71 (2008).
- [77] A. R. Liddle, Information criteria for astrophysical model selection, *Mon. Not. R. Astron. Soc.* **377**, L74 (2007).
- [78] M. Kunz, R. Trotta, and D. Parkinson, Measuring the effective complexity of cosmological models, *Phys. Rev. D* **74**, 023503 (2006).
- [79] A. Lewis, A. Challinor, and A. Lasenby, Efficient computation of CMB anisotropies in closed FRW models, *Astrophys. J.* **538**, 473 (2000).
- [80] <https://github.com/cmbant/CAMB>.
- [81] <https://github.com/dgrin1/axionCAMB>.
- [82] J. Lesgourgues and S. Pastor, Massive neutrinos and cosmology, *Phys. Rep.* **429**, 307 (2006).
- [83] Y. Y. Y. Wong, Neutrino mass in cosmology: Status and prospects, *Annu. Rev. Nucl. Part. Sci.* **61**, 69 (2011).
- [84] S. Agarwal and H. A. Feldman, The effect of massive neutrinos on the matter power spectrum, *Mon. Not. R. Astron. Soc.* **410**, 1647 (2011).
- [85] J. Liu and M. S. Madhavacheril, Constraining neutrino mass with the tomographic weak lensing one-point probability distribution function and power spectrum, *Phys. Rev. D* **99**, 083508 (2019).
- [86] KATRIN Collaboration, Improved Upper Limit on the Neutrino Mass from a Direct Kinematic Method by KATRIN, *Phys. Rev. Lett.* **123**, 221802 (2019).
- [87] A. E. Bayer, F. Villaescusa-Navarro, E. Massara, J. Liu, D. N. Spergel, L. Verde, B. D. Wandelt, M. Viel, and S. Ho, Detecting neutrino mass by combining matter clustering, halos, and voids, *Astrophys. J.* **919**, 24 (2021).
- [88] KATRIN Collaboration, Direct neutrino-mass measurement with sub-electronvolt sensitivity, *Nat. Phys.* **18**, 160 (2022).
- [89] Planck Collaboration, Planck 2018 results. V. CMB power spectra and likelihoods, *Astron. Astrophys.* **641**, A5 (2020).
- [90] R. Murgia, A. Merle, M. Viel, M. Totzauer, and A. Schneider, “Non-cold” dark matter at small scales: A general approach, *J. Cosmol. Astropart. Phys.* **11** (2017) 046.
- [91] R. Murgia, V. Iršič, and M. Viel, Novel constraints on noncold, nonthermal dark matter from Lyman- $\alpha$  forest data, *Phys. Rev. D* **98**, 083540 (2018).
- [92] M. Archidiacono, D. C. Hooper, R. Murgia, S. Bohr, J. Lesgourgues, and M. Viel, Constraining dark matter-dark radiation interactions with CMB, BAO, and Lyman- $\alpha$ , *J. Cosmol. Astropart. Phys.* **10** (2019) 055.